

1 Feasibility of robust estimates of ozone production rates 2 using a synergy of satellite observations, ground-based 3 remote sensing, and models

4
5 Amir H. Souri^{1,2*}, Gonzalo González Abad³, Glenn M. Wolfe¹, Tijl Verhoelst⁴, Corinne Vigouroux⁴,
6 Gaia Pinardi⁴, Steven Compernelle⁴, Bavo Langerock⁴, Bryan N. Duncan¹, Matthew S. Johnson⁵

7
8 ¹Atmospheric Chemistry and Dynamics Laboratory, NASA Goddard Space Flight Center, Greenbelt, MD,
9 USA

10 ²GESTAR II, Morgan State University, Baltimore, MD, USA

11 ³Atomic and Molecular Physics (AMP) Division, Center for Astrophysics | Harvard & Smithsonian,
12 Cambridge, MA, USA

13 ⁴Royal Belgian Institute for Space Aeronomy (BIRA-IASB), Ringlaan 3, 1180 Uccle, Belgium

14 ⁵Earth Science Division, NASA Ames Research Center, Moffett Field, CA, USA

15 * Corresponding author: a.souri@nasa.gov

16 17 **Abstract.**

18 Ozone pollution is secondarily produced through a complex, non-linear chemical process. Our
19 understanding of the spatiotemporal variations in photochemically produced ozone (i.e., PO₃) is limited to
20 sparse aircraft campaigns and chemical transport models, which often carry significant biases. Hence, we
21 present a novel satellite-derived PO₃ product informed by bias-corrected TROPOMI HCHO, NO₂, surface
22 albedo data, and various models. These data are integrated into a parameterization that relies on HCHO,
23 NO₂, HCHO/NO₂, jNO₂, and jO¹D. Despite its simplicity, it can reproduce ~90% of the variance in
24 observationally constrained PO₃ with minimal biases in moderately to highly polluted regions. We map PO₃
25 across various regions in July 2019 at a 0.1°×0.1° spatial resolution, revealing accelerated values (>8
26 ppbv/hr) in numerous cities throughout Asia and the Middle East, resulting from the elevated ozone
27 precursors and enhanced photochemistry. In Europe and the United States, such high levels are only
28 detected over Benelux, Los Angeles, and New York City. PO₃ maxima are seen in various seasons, attributed
29 to changes in photolysis rates, non-linear ozone chemistry, and fluctuations in HCHO and NO₂. Satellite
30 errors result in moderate errors (10-20%) of PO₃ estimates over cities on a monthly average, while these
31 errors exceed 50% in clean areas and under low light conditions. Using the current algorithm, we have
32 demonstrated that satellite data can provide valuable information for robust PO₃ estimation. This capability
33 expands future research through the application of data to address significant scientific questions about the
34 locally-produced PO₃ hotspots, seasonality, and long-term trends.

35 **1. Introduction**

36 Tropospheric ozone (O₃) is a secondary pollutant formed through complex photochemical reactions
37 involving various precursors, including nitrogen oxides (NO_x = NO + NO₂), volatile organic compounds

38 (VOCs), aerosols, and halogens (Kleinman et al., 2002, Simpson et al., 2015; Li et al., 2019). Ozone not
39 only poses significant risks to human health (Fleming et al., 2018) and agricultural productivity (Mills et
40 al., 2018) but also influences the radiation budget, thereby affecting the climate (Gaudel et al., 2018). To
41 mitigate the problem of elevated locally-produced ozone, it is crucial to understand the spatiotemporal
42 variability in ozone production rates (PO_3), defined as the number of ozone molecules generated through
43 secondary chemical pathways in the atmosphere. Comprehensive studies of ozone chemistry, informed by
44 observations, are typically confined to observationally-rich air quality campaigns (e.g., Cazorla et al., 2012;
45 Ren et al., 2013; Mazzuca et al.; 2016; Souri et al., 2020a; Schroeder et al., 2020; Brune et al., 2022; Wolfe
46 et al., 2022; Souri et al., 2023), which are sparse in time and space.

47 Significant advancements have been achieved in using various measurable ozone indicators to
48 simplify the non-linear relationship between PO_3 and NO_x and VOCs into linear forms (Sillman and He,
49 2002). These forms include NO_x -sensitive (where PO_3 is sensitive to NO_x), VOC-sensitive (where PO_3 is
50 sensitive to VOCs), and the transitional regimes (where PO_3 is sensitive to both NO_x and VOCs). Among
51 the numerous proposed indicators, the ratio of formaldehyde (HCHO) to nitrogen dioxide (NO_2) (known as
52 FNR) has gained popularity (Tonnesen and Dennis, 2000a,b), despite its less effective performance
53 compared to the H_2O_2/HNO_3 ratio in fully explaining the HO_x-RO_x cycle (Sillman and He, 2002; Souri et
54 al., 2023). The preference for FNR stems from the fact that both quantities can be informed by UV-Vis
55 radiance data, such as those provided by the Ozone Monitoring Instrument (OMI) and the TROPospheric
56 Monitoring Instrument (TROPOMI) (Martin et al., 2005; Duncan et al., 2010; Choi et al., 2012; Choi and
57 Souri, 2015a, b; Jin and Holloway, 2015; Jin et al., 2017; Schroeder et al., 2017; Souri et al., 2017; Jeon et
58 al., 2018; Tao et al., 2022). Several limitations associated with the application of satellite-based FNR have
59 been identified such as i) the inherent limitation of understanding the radical termination in the RO_x-HO_x
60 cycle (Souri et al., 2020a; Souri et al., 2023), ii) the challenges associated with converting the column
61 vertical density to the near-surface concentrations (Jin et al., 2017; Schroeder et al., 2017; Souri et al.,
62 2023), iii) spatial representativity associated with large satellite pixels (Souri et al., 2020a, 2023; Johnson
63 et al., 2023), and iv) the retrieval errors (Souri et al., 2023; Johnson et al., 2023). Souri et al. (2023)
64 concluded that the retrieval errors make up the largest portion of total errors associated with FNR. These
65 errors are becoming smaller with better sensor designs, retrieval algorithms, and calibration over time.

66 While the characterization of ozone regimes offers valuable insights for regulators to prioritize
67 effective emission control strategies, it does not provide information about the magnitude of PO_3 or the
68 absolute quantities of PO_3 derivatives relative to its precursors. Consequently, chemical transport models
69 under various emission scenarios are typically employed (e.g., Pan et al., 2019). These models allow for
70 the execution of process-based scenarios to elucidate the response of PO_3 to different emissions and can
71 simulate four-dimensional PO_3 data. However, the results of these simulations are based on various
72 assumptions and inputs, which carry significant uncertainties. Therefore, it is essential to optimize some of
73 the models' prognostic inputs using observations through inverse modeling/data assimilation. The primary
74 advantage of inverse modeling/data assimilation using satellite observations is its ability to account for
75 satellite errors and eliminate the influence of the a priori profile, thereby carrying only radiance information
76 into the emission estimation. Numerous studies have utilized satellite observations to constrain NO_x and
77 VOC emissions for various applications (e.g., Stavrou et al., 2016; Souri et al., 2016; Miyazaki et al.,
78 2017; Souri et al., 2017; Souri et al., 2020b; Souri et al., 2021; Choi et al., 2022; DiMaria et al., 2023).
79 Souri et al. (2020b) made an early attempt to simultaneously optimize both NO_x and VOC emissions over
80 East Asia for a more accurate representation of PO_3 . Their joint-inversion was able to account for the
81 intertwined relationship between HCHO- NO_x and NO_2 -VOC. However, the execution of chemical transport
82 models optimized by multiple satellite observations remains prohibitively expensive, particularly for high-
83 resolution domains demanded by regulatory agencies.

84 Data-driven methods for estimating PO_3 can become as a more cost-effective alternative to physics-
85 based methods. While using constrained chemical transport models provides a relatively robust framework
86 grounded in some explicit governing equations, they require extensive computation resources and expertise.

87 Conversely, data-driven algorithms make use of large datasets to identify patterns and make predictions
88 with much reduced computational expenses. However, it is important to recognize that data-driven
89 algorithms lack the ability to provide solid physical interpretability and generalizability. Despite this
90 fundamental limitation, they are sensible tools for applications where rapid analysis over a wide spatial
91 coverage is prioritized. Data-driven parameterizations for several components of atmospheric chemistry
92 such as OH (Anderson et al., 2022) and dry deposition (Silva et al., 2019) have been crafted for this reason.
93 However, to our best knowledge, Chatfield et al. (2010) and Souri et al. (2023) are the only studies that
94 attempted to empirically parameterize PO₃ using the information of HCHO and NO₂ mixing ratios.

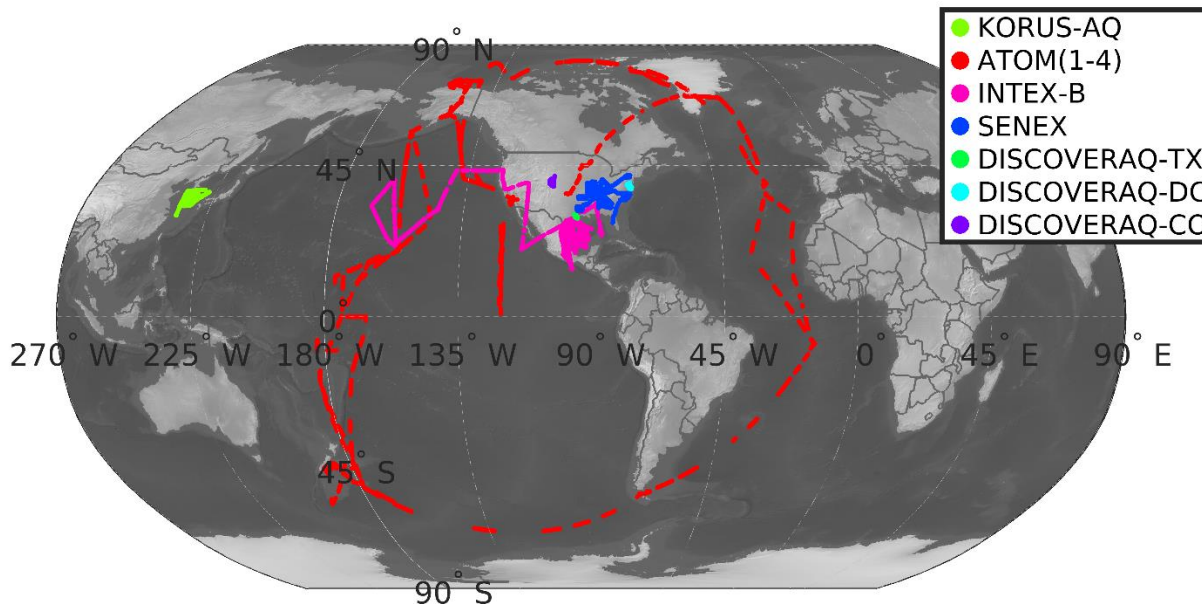
95 Inspired by those works, we developed a novel product using TROPOMI observations in
96 conjunction with ground-based remote sensing and atmospheric models to estimate PO₃ and associated
97 errors within the planetary boundary layer (PBL) across the globe. This enabled us to map PO₃ across
98 various regions at fine scales (i.e., 0.1°×0.1°) for the first time.

99 **2. Data**

100 **2.1. Aircraft**

101 To study PO₃, we use various aircraft observations from several National Aeronautics and Space
102 Administration (NASA) and National Oceanic and Atmospheric Administration (NOAA) atmospheric
103 composition campaigns. We have selected three sets of aircraft campaigns for the purpose of PO₃
104 estimation, targeting: i) urban/suburban air quality, including Deriving Information on Surface Conditions
105 from Column and Vertically Resolved Observations Relevant to Air Quality (DISCOVER-AQ) Baltimore-
106 Washington (2011), DISCOVER-AQ Houston-Texas (2013), DISCOVER-AQ Colorado (2014), and the
107 Korea United States Air Quality Study (KORUS-AQ) (2016) (Crawford et al., 2021); ii) remote areas
108 including Atmospheric Tomography Mission (ATOM) (Thompson et al., 2022) and Intercontinental
109 Chemical Transport Experiment (INTEX) phase B (Singh et al., 2009); iii) a mixture of isoprene-rich
110 environment and large emitters, including SENEX (Southeast Nexus) (Warneke et al., 2016). Figure 1
111 shows the location of these campaigns. Inspired by the study of Miller and Brune (2022), we list their
112 “when, where, why” characteristics in Table S1.

113 For aircraft campaigns targeting polluted areas, including DISCOVERs, KORUS-AQ, SENEX,
114 and SEAC4RS, we use 10-sec merged data, whereas, for other measurements taken in relatively remote
115 areas, such as INTEX-B and ATOMs, we used 30-sec merged data. A more detailed description of the
116 measurements is provided in Section 3.2. We exclude times with no measurements of NO, NO₂, or HCHO.
117 The concentrations of OH and HO₂ were only measured during INTEX-B, ATOMs, and KORUS-AQ.
118 Likewise, we void any data points lacking either HO₂ or OH measurements. There are frequent gaps in
119 some measurements, especially for VOCs, because of instrument issues or measurement techniques.
120 Following Souri et al. (2020a), Miller and Brune (2020), Souri et al. (2023), and Bottorff et al. (2023), we
121 fill the gaps in measurements using a linear interpolation method with no extrapolation allowed beyond 15
122 minutes. We drop any remaining gaps from the analysis. To better capture the rapid fluctuation of VOCs,
123 we pick the PTR-TOF-MS instrument with high temporal resolution over the whole air sampler (WAS)
124 when both instruments have measured the same quantity. Regarding the INTEX-B campaign, we drop
125 isoprene observation due to infrequent samples downgrading the performance of our box model.



126
 127 **Figure 1.** The location of seven different atmospheric composition aircraft campaigns used in this study.

128 **2.2. TROPOMI NO_2 and HCHO**

129 We use the recently reprocessed daily level-2 (L2) TROPOMI tropospheric NO_2 and total HCHO
 130 columns (v2.4) derived from UV-visible radiances onboard the European Space Agency’s (ESA’s) Sentinel-
 131 5 Precursor (S5P) spacecraft (~328-496 nm) (Veefkind et al., 2012, De Smedt et al. 2021; van Geffen et al.,
 132 2022). This sensor has been operational since May 2018, providing global coverage of NO_2 and HCHO at
 133 ~1:30 local standard time at the Equator. Since NO_2 and HCHO are optically thin absorbers in the UV-
 134 Visible, meaning their concentrations do not substantially affect the sensitivity of the radiance to the optical
 135 thickness of the absorber, the retrieval follows the conventional two-step algorithm involving spectral fitting
 136 for Slant Column Density (SCD) retrieval and Air Mass Factor (AMF) calculations for SCD to Vertical
 137 Column Density (VCD) conversion. The product has a spatial resolution of 7.2 km (5.6 km as of August
 138 2019) by 3.6 km at nadir. To remove unfit measurements, we use the provided quality flag (*q_value*) and
 139 choose only those above 0.75 for NO_2 and 0.5 for HCHO. As the L2 product does not come in a regular
 140 grid, we use a mass-conserved regridding technique based on barycentric linear interpolation to map out
 141 the data onto a $0.1^\circ \times 0.1^\circ$ regular grid.

142 van Geffen et al. (2022) demonstrated that the reprocessed TROPOMI tropospheric NO_2 columns
 143 exhibit a good level of correspondence with those obtained from ground-based MAX-DOAS sky
 144 spectrometers, with a correlation of 0.88 and a median bias of -23%, improving on the older product
 145 versions which were biased low by about 30% with respect to ground-based measurements at polluted sites
 146 (Verhoelst et al., 2021). More information about new modifications and their impacts on the retrieval can
 147 be found in van Geffen et al. (2022).

148 The studies of Vigouroux et al. (2020) and De Smedt et al. (2021) validated the reprocessed
 149 monthly-mean TROPOMI HCHO columns against FTIR and MAX-DOAS observations and found a good
 150 correlation above 0.8 with a negative bias of 20-30% for polluted sites. The bias tends to be slightly positive
 151 or neutral over clean sites.

152 **2.2.1. Error characterization of TROPOMI NO_2 and HCHO using ground-based retrievals**

153 To propagate TROPOMI retrieval errors to the PO_3 product and to remove potential biases, we
 154 assume three origins for errors: i) random errors resulting from instrument noise, ii) a fixed additive

155 component that is magnitude-independent (i.e., a uniform offset persisting over all pixels), and iii)
 156 unresolved systematic biases that are multiplicative and irreducible by oversampling. The first component
 157 is derived from the column precision variable provided along with the L2 product. In the spatial domain,
 158 we interpolate the squares of this error the same of way we map the irregular L2 pixels into the $0.1^\circ \times 0.1^\circ$
 159 regular grid. Moreover, we average the random errors over a month to reduce random noise by the squared
 160 number of pixels available at the same location (Eq. 3). Two other errors are determined by comparing
 161 FTIR (for HCHO) and MAX-DOAS (for tropospheric NO_2) with TROPOMI data (Section 4.3.3). Detailed
 162 explanation of how these datasets are paired can be found in Vigouroux et al. (2020) and Verhoelst et al.
 163 (2021). Both datasets cover the period of 2018-2023.

164 To achieve an optimal linear fit ($y = ax + b + \varepsilon$) between the paired observations, where a and b
 165 are slope and offset to be determined, we follow a Monte-Carlo Chi-squares minimization such that $\chi^2 =$
 166 $\sum \frac{[y-f(x_i,a,b)]^2}{\sigma_y^2 + a^2 \sigma_x^2}$ is minimized. In this equation, σ_y^2 and σ_x^2 are the variances of y (TROPOMI) and x (the
 167 benchmark, here FTIR or MAX-DOAS), respectively; i is the subscript refers to i -th observation point, and
 168 f is the proposed linear fit subject to optimization. In terms of TROPOMI NO_2 and HCHO, the errors are
 169 populated based on the L2 information. According to Verhoelst et al. (2021), a fixed error of 30% is assumed
 170 for MAX-DOAS NO_2 observations whose values are above $1.4 \times 10^{15} \text{ molec/cm}^2$. Because of the detection
 171 limit of MAX-DOAS NO_2 , we set errors for values below that threshold to $1.4 \times 10^{15} \text{ molec/cm}^2$. The FTIR
 172 retrieval errors described in Vigouroux et al. (2020) were used to populate the errors associated with this
 173 benchmark. The minimization is performed 10000 times, each with a set of random perturbations of x and
 174 y within their respective prescribed errors. This approach allows us to assess the robustness of the estimates
 175 across the range of errors associated with each data point.

176 The offset (a uniform additive term) and the slope (multiplicative error) drawn from the ground
 177 validation are used to correct the biases associated with TROPOMI via:

$$VCD_{bias-corrected} = \frac{VCD_{original} - offset}{slope} \quad (1)$$

178 Since there are errors associated with this adjustment resulting from instrument and representation errors,
 179 we augment errors of the slope and offset to the total error and label them constant errors (e_{const}) via:

$$e_{const}^2 = e_{offset}^2 + e_{slope}^2 \times VCD_{bias-corrected}^2 \quad (2)$$

180 where e_{offset}^2 and e_{slope}^2 are squares of errors of offset and slope calculated from the linear regression (Eq.
 181 1). Ultimately, the sum of all three errors constitutes the total errors given:

$$e^2 = e_{const}^2 + \frac{1}{m^2} \sum_{i=1}^m e_{random,i}^2 \quad (3)$$

182 where m is the number of samples for a given grid and timeframe and e_{random}^2 is squares of random errors.

183 **2.3. TROPOMI Surface Albedo**

184 To account for the effect of surface albedo on photolysis rates (Section 2.5), we use a newly
 185 developed algorithm based on the directionally dependent Lambertian-equivalent reflectivity (DLER) UV
 186 surface albedo climatology made from TROPOMI radiance (Tilstra et al., 2024). This new database
 187 leverages 60 months of TROPOMI reprocessed radiance and is produced at the grid resolution of
 188 $0.125^\circ \times 0.125^\circ$. The product has outperformed traditional LER products such as OMI when both were
 189 compared to MODIS surface the bidirectional reflectance distribution function (BRDF) results (Tilstra et
 190 al., 2024).

191 2.4. MERRA2-GMI

192 To convert vertical column densities of HCHO and NO₂ from TROPOMI to their volume mixing
193 ratios in the PBL region, we use the MERRA2-GMI (M2GMI) model ([https://acd-
194 ext.gsfc.nasa.gov/Projects/GEOSCCM/MERRA2GMI/](https://acd-ext.gsfc.nasa.gov/Projects/GEOSCCM/MERRA2GMI/), last access: 10 Sep 2023). This model is NASA’s
195 Goddard Earth Observing System (GEOS) Chemistry-Climate Model (CCM) run spanning for the period
196 of 1980-2019, exploiting MERRA2 (Modern Era Retrospective analysis for Research and Applications) to
197 constrain meteorological fields (Orbe et al., 2017). The model uses the Global Modeling Initiative (GMI)
198 chemical mechanism (Duncan et al., 2007; Strahan et al., 2007), which involves over 120 species and 400
199 reactions. It has a resolution of approximately 0.625° longitude by 0.5° latitude with 72 vertical layers
200 stretching from the surface up to 0.1 hPa. Additional information about the configuration of this model can
201 be found in Strode et al. (2019). To carry out the conversion, we apply the following conversion factor (γ)
202 to the TROPOMI VCDs:

$$\gamma = \frac{\bar{q}_{PBLH}}{\frac{NA}{g \times Mair} \sum q dp} \quad (4)$$

203 where \bar{q}_{PBLH} is the average of the target trace gas mixing ratios in the PBLH, g is the acceleration
204 of the gravity (assumed 9.81 m/s²), NA is the Avogadro constant, $Mair$ is the air molecular weight
205 (assumed 28.96 g/mol), q is the target trace gas mixing ratio at a given altitude, and dp is the
206 thickness of each model vertical grid box in hPa. The denominator in Eq. 4 represents the modeled
207 VCD. We integrate modeled partial VCDs up to top of the atmosphere for HCHO, and up to the
208 tropopause pressure layer for NO₂.

209 2.5. TUV NCAR Photolysis Rates Look-up Table

210 To estimate photolysis rates, JNO₂ (NO₂+hv) and JO¹D (O₃+hv), we use a comprehensive look-up
211 table provided by the F0AM model (Section 3.2) created for clear-sky conditions. This look-up table is
212 based on the calculation of more than 20,064 solar spectra over a wide range of solar zenith angle (SZA)
213 (the range [0, 90] in steps of 5°), altitude (the range [0, 15] in steps of 1 km), overhead total ozone column
214 (the range [100, 600] in steps of 50 DU), and surface UV albedo (the range [0, 1] in steps of 0.2) using
215 NCAR’s Tropospheric Ultraviolet and Visible radiation model (TUV v5.2) and cross sections and quantum
216 yields from IUPAC and JPL (Wolfe et al., 2016). The L2 TROPOMI granule information populates SZA,
217 surface elevation, and surface UV albedo, while overhead total ozone columns are obtained from MERRA2-
218 GMI (Section 2.4) which is found to agree well with satellite observations (Souri et al., 2024). Any values
219 between these tables are bilinearly interpolated for a smoother result.

220 3. Methods

221 In this section, we begin by discussing a robust regression model specifically developed for
222 feature selection in the parameterization of PO₃. We then describe the training dataset created for this
223 purpose. Following that, we introduce a clustering technique utilized to organize the training data, which
224 enables us to identify the key drivers of PO₃ variability. Finally, we provide a comprehensive overview of
225 the PO₃ estimates algorithm by integrating data from the TROPOMI retrievals, ground-based remote
226 sensing, and various models.

227 3.1. LASSO

228 Through the use of multi-linear regression models, it is possible to establish a simple but robust
229 relationship between multiple variables and a target. However, when dealing with a large number of
230 variables, there is a chance of introducing overfitting issues. This can lead to predictions that are either
231 overly optimistic or unrealistic for values outside of the training dataset. To avoid this, it is recommended

232 to simplify the model by removing variables that are loosely connected with the target or highly correlated
233 with others. This process is known as "model shrinkage" and can narrow down the number of possible
234 solutions (i.e., variance) at the cost of increasing the biases between the observed target and predictions.
235 Ideally, we want a model that minimizes the sum of the bias and the variance. To achieve this, we can use
236 LASSO (least absolute shrinkage and selection operator) (Tibshirani, 1996). They consider a regression,

$$Y = X\beta + \alpha + \varepsilon \quad (5)$$

237 with response $Y = (y_1, \dots, y_n)^T$, $n \times p$ explanatory variables X , coefficients $\beta = (\beta_1, \dots, \beta_p)^T$, an intercept α ,
238 and noise variables $\varepsilon = (\varepsilon_1, \dots, \varepsilon_n)^T$. n is the number of data points, and p is the number of explanatory
239 variables. We can label the regression model sparse when many of β values are zero, and we can label it
240 high dimensional when $p \gg n$. LASSO attempts to select variables such that the following cost function is
241 minimized:

$$(\hat{\alpha}, \hat{\beta}) = \underset{\alpha, \beta}{\operatorname{argmin}} \left\{ \|Y - X\beta - \alpha\|_2 + \lambda \sum_{i=1}^p |\beta_i| \right\} \quad (6)$$

242 where $\hat{\alpha}$ and $\hat{\beta}$ are optimized intercept and coefficients, λ is a non-negative regularization factor subject to
243 tuning, i is the subscript of the i -th explanatory variable, and $\|\cdot\|_2$ is the L2-norm operator. The first term
244 on the right side of Eq.6 minimizes the squares of the residuals, whereas the second term reduces the sum
245 of absolute value of coefficients resulting in a simpler model with fewer parameters. Without the second
246 term, the regression model becomes an ordinary least-squares estimation. The most critical element here is
247 λ . A large λ results in more aggressive regularization leading to more model shrinkage, whereas a small
248 value preserves a high dimensional model. To optimize this value, we discretize λ in 100 values between
249 10^{-4} up to 10^1 , divide the training dataset into 10 folds (i.e., splitting the dataset into equal size segments),
250 determine the average of cross-validated error prediction among all folds, and find λ that yields the smallest
251 error. The final solution ensures a balanced model with respect to model parsimony and bias. All
252 explanatory variables are standardized during the regularization procedure such that their mean becomes
253 zero and their standard deviation one.

254 **3.2. Photochemical box modeling**

255 To produce training data sets for LASSO-based PO_3 estimation, we use the Framework for 0-D
256 Atmospheric Modeling (F0AM) v4 box model (Wolfe et al., 2016), constrained by a wide range of
257 observations. These observations ensure that the model achieves a realistic range of values found in the
258 atmosphere. We follow past setups which apply the Carbon Bond 6 (CB06, r2) chemical mechanism in
259 F0AM (Souri et al., 2020a; Souri et al., 2023). The model is constrained by aircraft data, including
260 meteorology, photolysis rates, and trace gas concentrations. The model configuration and observations used
261 are listed in Table S2.

262 Once the model is initialized and held constant with respect to a wide range of constraining
263 quantities, it runs at 30 minutes integration time cycling for five days to approach a steady-state
264 environment. Several key compounds including OH, HO_2 , HCHO, PAN, NO, and NO_2 are initialized with
265 aircraft observations but they are left free to cycle with incoming solar radiation variability. These
266 compounds play a crucial role in validating the efficacy of model performance as well as the adequacy of
267 observations used as constraints. In particular, allowing HCHO to vary freely enables us to assess whether
268 our mechanism for VOC treatment, steady-state, and the number of measured VOCs suffice to reproduce
269 its concentrations reasonably. Although the individual concentration of NO_2 and NO are not constrained,
270 we constrain total NO_x ($\text{NO} + \text{NO}_2$). Not all aircraft campaigns measured all photolysis rates included in the
271 chemical mechanism. We first initialize the photolysis rates included in CB06 using the look-up-tables
272 described in Section 2.5. If any photolysis reaction rates in CB06 were measured, we replace the initial

273 guess with the observed values. For those reactions with photolysis rates not been measured, we apply a
274 scaling factor made of the average of the ratio of the observed J-values to the modeled J-values. This
275 approach is a sensible choice for accounting for large particles such as clouds, as their extinction coefficient
276 is somewhat non-selective in the UV-Vis range; however, applying a wavelength-independent scaling factor
277 may introduce some biases for optically complex environments introduced by aerosols.

278 It is essential to acknowledge the inherent limitations of a box model in our research. The model
279 does not consider the diverse physical loss pathways that trace gases may undergo, including deposition
280 and transport. As a result, we have simplified the physical loss by employing a first-order dilution rate set
281 to $1/86400 \text{ s}^{-1}$, equivalent to a lifetime of 24 hours. This approach ensures that unconstrained trace gases
282 that take longer to break down do not accumulate over time. Exact knowledge of dilution factors requires
283 knowing molecular and turbulent diffusion, entrainment and detrainment, and deposition rates, all of which
284 are unknown at the micro-scale level of aircraft observations. Nonetheless, studies of Brune et al. (2022)
285 and Sourì et al. (2023) showed that HO_2 , OH , NO_x , and HCHO are relatively immune to the choice of the
286 dilution factor, whereas RO_2 mixing ratios can depart introducing some biases in PO_3 estimates.

287 We determine simulated PO_3 by:

$$PO_3 = FO_3 - LO_3 \quad (7)$$

288 where LO_3 is all possible chemical loss pathways of ozone (negative stoichiometric multiplier matrix) and
289 FO_3 is all possible chemical pathways producing ozone molecules (positive stoichiometric multiplier
290 matrix). This calculation is theoretically equivalent to a value obtained from a chemical solver quantifying
291 the number of ozone molecules produced/lost for each model timestep. The adoption of Eq.7 facilitates the
292 direct comparison of PO_3 estimations with those derived from other models, including CTM-based results
293 (see Figure 10 in Sourì et al., 2021). Furthermore, it allows for a seamless integration of these estimates
294 into Lagrangian transport models for ozone forecasting purposes.

295 3.3. Clustering

296 The aim of using a classifier to group the large quantity and types of aircraft data into similar
297 features is to allow us to study the primary contributors to PO_3 under different chemical, solar, and
298 meteorological conditions. Additionally, this approach will help us understand the range of atmospheric
299 conditions included in the training dataset. To accomplish this, we employ a widely-used technique known
300 as k -means, which has been used in a variety of applications (e.g., Beddows et al., 2009; Sourì et al., 2016b;
301 Govender and Sivakumar, 2020). In this approach, centroids are distributed randomly throughout a multi-
302 dimensional dataset, with each centroid representing a distinct class. The algorithm proceeds to assign a
303 label to each data point by identifying its closest Euclidean distance to the centroids. Following the labeling
304 of all data points, the algorithm updates the centroids based on the means of the newly-labeled group. This
305 process continues iteratively until there is minimal change in the location of the centroids. It is worth noting
306 that k -means does not guarantee an optimal solution, so we reinitialize the classification 1000 times with a
307 new set of initial centroids. We select the result with the lowest value for the sum of the Euclidean distance
308 among data points and centroids to ensure the outcomes are not influenced by random seeding.

309 Redundant features in the input can significantly compromise the effectiveness of the classification,
310 so we apply principal component analysis (PCA) to the matrix of datasets (Z) with n data points and p
311 features to reduce the dimension to a PCA-transformed matrix of Z (Z') with the dimension $n \times q$, where
312 $q < p$. Despite this reduction in dimension, Z' preserves a significant variance in Z , helping us to overcome
313 the issues of dimensionality or overfitting.

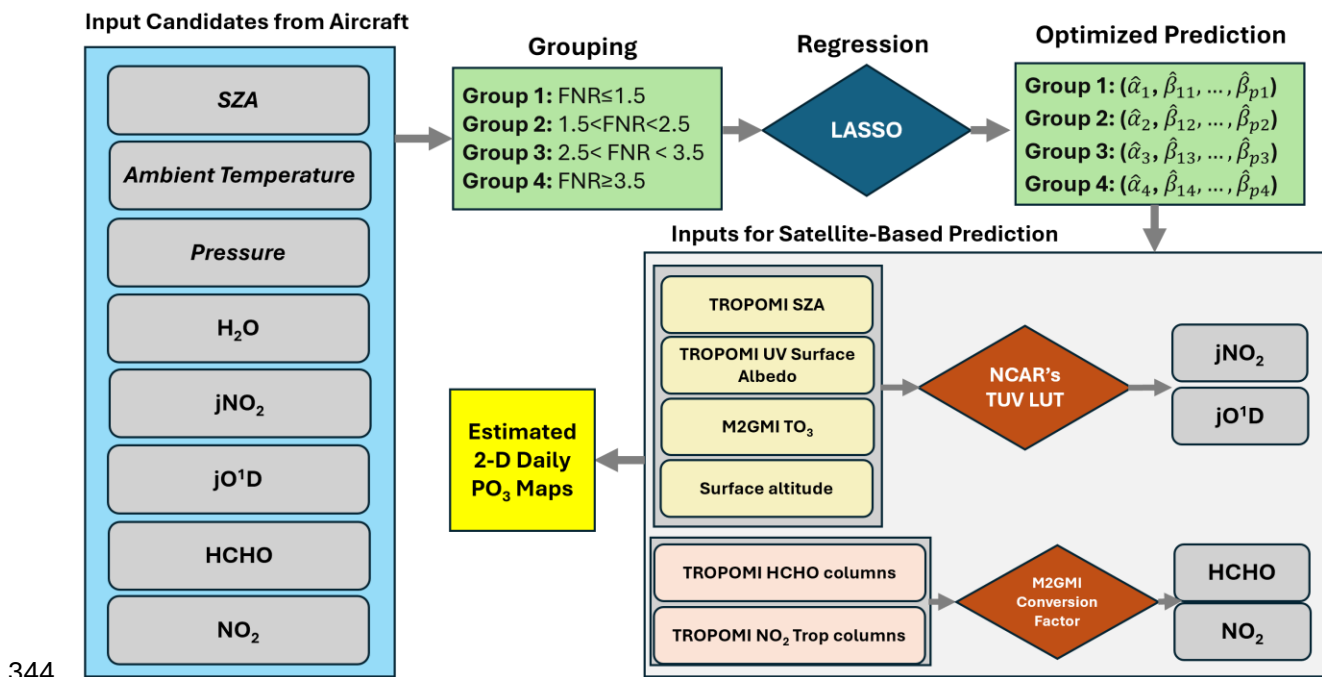
314 We select 11 features simulated by the F0AM model, many of which are set to the observed values,
315 or their precursors are observationally-constrained. These features are SZA, HCHO/NO_2 , $\text{HCHO} \times \text{NO}_2$,
316 HCHO , NO_2 , pressure, temperature, $j\text{NO}_2$, $j\text{O}^1\text{D}$, H_2O , and NO_2/NO_y ($\text{NO}_y = \text{NO} + \text{NO}_2 + \text{PAN} + \text{HNO}_3 + \text{alkyl}$)

317 nitrate +N₂O₅). There are indeed correlations among these features such as SZA and jNO₂, or HCHO and
 318 HCHO×NO₂; nonetheless, we have used PCA to eliminate the possibility of these correlated factors causing
 319 overfitting issues.

320 3.4. The estimation of PO₃

321 In order to predict PO₃, we have developed empirical equations using LASSO to link PO₃ with
 322 various relevant prognostic candidates related to ozone chemistry. A schematic presentation on how this
 323 estimation can be done to provide daily PO₃ maps at the TROPOMI revisit time across the globe is shown
 324 in Figure 2. It is important to note that relying solely on linear regressions for a non-linear problem is not a
 325 viable approach. To address this, we have divided the data points into four distinct groups based on FNR
 326 values, meaning we divide a non-linear realm into smaller linear segments (i.e., an empirical linearization).
 327 In a study by Souri et al. (2023), a wide range of aircraft observations and box model results were used to
 328 determine that FNR~1.7 was a universal threshold for separating NO_x-sensitive from VOC-sensitive
 329 regimes. We have found that by breaking down the datapoints into slightly weaker or stronger variations of
 330 the regimes, we can improve the accuracy of our results. As a result, we have established four distinct
 331 groups: VOC-sensitive (FNR<1.5), transitions (1.5<FNR<2.5 and 2.5<FNR<3.5), and NO_x-sensitive
 332 (FNR>3.5). The coefficients and intercepts based on the LASSO regressions for each group were computed
 333 separately. From a long list of explanatory parameters, we selected SZA, temperature, pressure, H₂O, jNO₂,
 334 jO¹D, HCHO, and NO₂ as the most sensible candidates. The reasoning behind this selection will be
 335 discussed in Section 4.2.

336 Once the LASSO parameters are determined, we apply the linear functions to variables
 337 modeled/observed in the PBL region. We show that the LASSO method votes for dropping SZA,
 338 temperature, water vapor, and pressure as they do not provide significant information on PO₃ compared to
 339 the rest. As for jNO₂ and jO¹D, we use the TUV NCAR’s LUT described in Section 2.5. HCHO and NO₂
 340 are derived by converting the bias-corrected TROPOMI VCDs into PBL mixing ratios using MERRA2-
 341 GMI described in Section 2.4. To carry out the conversion, we multiply the satellite VCDs by the ratio of
 342 averaged modeled mixing ratios of a target gas (i.e., NO₂ or HCHO) in the PBL region divided by modeled
 343 VCDs (Section 2.4). The PBL field also comes from MERRA2-GMI.



344

345 **Figure 2.** Schematic illustration of daily PO₃ estimation calculated in this study. This process consists of
346 two major steps: formulating PO₃ as a function of various prognostic inputs derived from the box model
347 results, and predicting PO₃ based on optimized features/coefficients suggested by LASSO and using
348 information obtained from TROPOMI, TUV, and M2GMI.

349 **4. Results and Discussion**

350 **4.1. Box Model Validation**

351 In order to assess the accuracy of the assumptions used in the box model's setup, which involves
352 factors such as chemical mechanism, dilution rate, and photolysis rate correction, we will compare the
353 simulated values of HCHO, NO₂, NO, PAN, HO₂, and OH with their actual measured values. This
354 comparison will help us determine if our model falls within an acceptable range of errors as seen in other
355 reputable photochemical box modeling studies. This comparison is represented in Figure 3, which displays
356 a scatterplot of the data collected from all seven aircraft campaigns. A discussion on each parameter follows:

357 HCHO – The box model is proficient in capturing over 77% of variance in observations with less
358 than 15% absolute bias. While many box modeling studies prefer to have this compound constrained to
359 potentially enhance the representation of HO_x, it comes with the trade-off of hindering us from validating
360 the number/quality of observed HCHO precursors and/or the VOC treatment. Besides the study of Souri et
361 al. (2023), Marvin et al. (2017) is one of the few studies that did not constrain this compound to verify the
362 efficacy of different pathways involved in HCHO formation and loss simulated by various chemical
363 mechanisms. Marvin et al. (2017) reproduced HCHO formation during the SENEX campaign using the
364 CB06 mechanism with a R²=0.66 and a bias of 32% at 1-min averaged samples. Compared to that study,
365 we recreate 86% variance in observed HCHO during the same campaign with a bias of 23% (Figure S1) at
366 10-sec averaged samples. The remaining unresolved variance can be attributed to an incomplete list of VOC
367 measurements for several campaigns including DISCOVER-AQs and errors of VOCs measurements. It is
368 unlikely for the chemical mechanism to be reason for this, as Marvin et al. (2017) did not observe substantial
369 differences in R² values among various chemical mechanisms including the near-explicit MCM. A mild
370 underestimation of HCHO could be likely due to the steady-state assumption, fixed arbitrary dilution factor,
371 or uncertain isoprene chemistry (Archibald et al., 2000; Wolfe et al., 2016; Marvin et al., 2017).

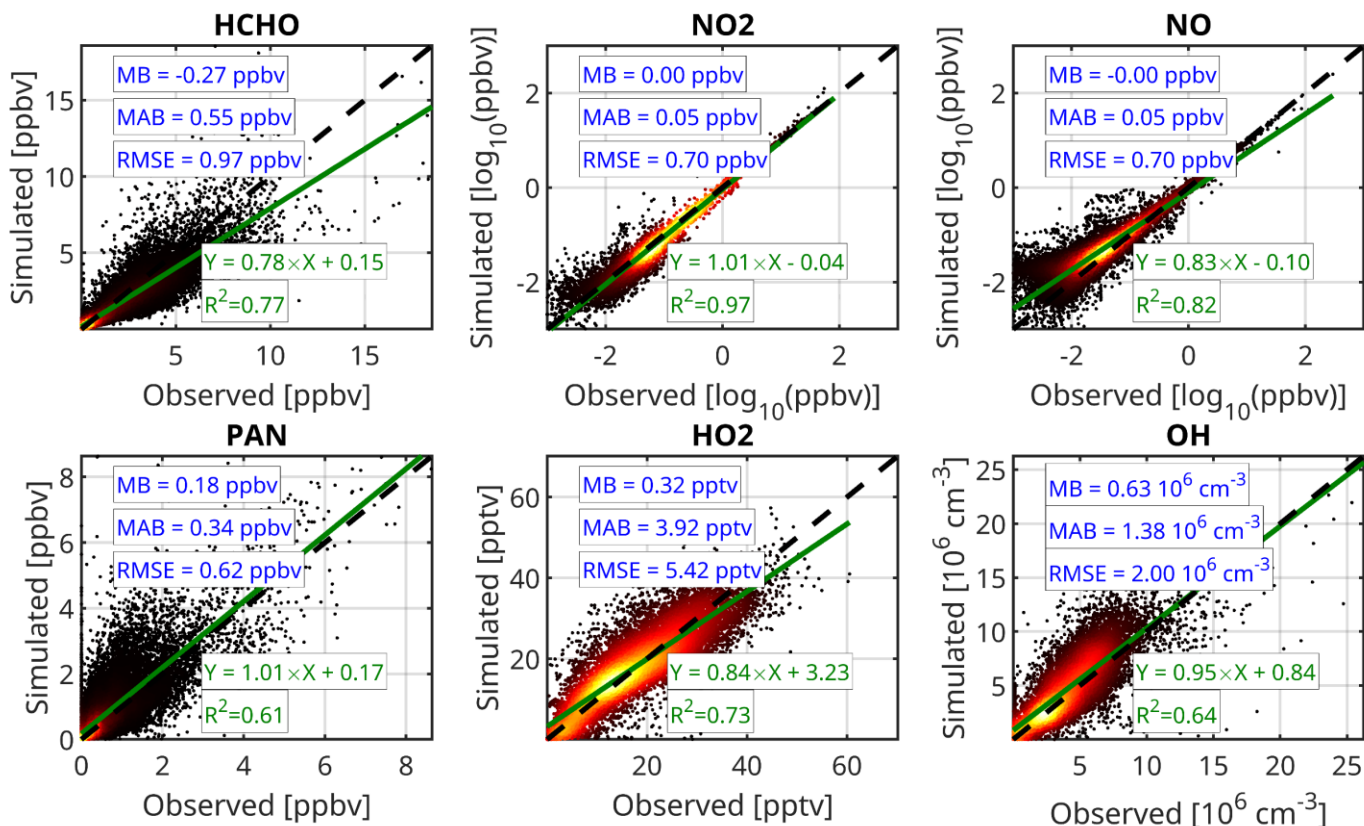
372 NO₂ and NO – Comparisons for both species demonstrate a high degree of correspondence for
373 values above 0.1 ppbv. Nonetheless, we have noted a substantial amount of fluctuation in the simulations
374 in clean regions, particularly for NO. While we cannot rule out the possibility of chemical mechanism
375 uncertainty contributing to this deviation, the reported measurement errors for NO₂ and NO are usually
376 ±0.05 ppbv and ±0.1 ppbv, respectively. Consequently, it is likely that the measurements error resulted in
377 more spread in comparison. In particular, Shah et al. (2023) found that these measurements could be
378 contaminated by various reactive nitrogen species in remote regions precluding a robust validation of
379 atmospheric models.

380 PAN – Our model reproduced 61% of the variance observed in PAN with a marginal absolute bias.
381 According to Xu et al. (2021), the presence of oxygenated VOCs, particularly acetaldehyde, and the
382 NO/NO₂ ratio are key factors controlling PAN levels. While we have constrained acetaldehyde, variations
383 in the NO/NO₂ ratio in heavily polluted regions (where NO_x levels exceed 1 ppbv) could potentially lead
384 to biases in PAN simulations. Furthermore, our model's dilution factor has been arbitrarily set, and it is
385 possible that any bias caused by this factor has been canceled out by other effects, leading to seemingly
386 bias-free performance. However, Souri et al. (2023) showed that an incorrect dilution factor can
387 significantly impact PAN performance, causing a sharp decline in R² resulting in a value below 30%.
388 Therefore, the fact that our box model has performed well with respect to PAN could be an indication that
389 our choice of the dilution factor is reasonable.

390 HO₂ and OH – Based on our analysis of HO₂ and OH simulations during KORUS-AQ, INTEX-B,
391 and ATOMs, we have found a reasonable level of correspondence ($R^2 > 0.6$) with the performance in
392 previous studies conducted by Sourì et al. (2020), Brune et al. (2022), Miller and Brune (2022), and Sourì
393 et al. (2023) that focused on some of these campaigns. Although the box model OH simulations reported in
394 Brune et al. (2019) during ATOMs seemed to be better than ours ($R^2 \sim 0.8$ vs $R^2 \sim 0.6$), it is important to
395 consider that their observations were averaged over 1-minute intervals as opposed to our 30-second
396 intervals. It should also be noted that there can be large errors in ATHOS HO_x measurements of up to $\pm 40\%$
397 (Miller et al., 2022), so recreating the exact variance in the observations should not be the main objective.
398 Nonetheless, the performance of our simulations in terms of HO_x compared to observations suggests that
399 the number of measured compounds and chemical mechanisms used in the model was effective. Our
400 model's performance with respect to HO_x is comparable to more sophisticated mechanisms that encompass
401 a larger number of measured species (Brune et al., 2022; Miller and Brune, 2022).

402 Overall, while there are inevitably some differences between the box model results and
403 observations, they are consistent with what other studies have found in similar aircraft campaigns. Our
404 extensive box model results, which consider a variety of meteorological, chemical, and photolysis rates,
405 demonstrate satisfactory results for unconstrained compounds across a wide range of atmospheric
406 conditions. This suggests that our training dataset from the box model is a reliable source for understanding
407 local PO₃.

408 It is important to note that even if a simulated data point does not match up perfectly with actual
409 observations, it still plays a role in establishing PO₃ and other explanatory variables. Hypothetically, one
410 can generate synthetic training data points by running the box model under random numbers for the inputs;
411 but only a fraction of those can be truly observed in nature. Therefore, a mild outlier in our training dataset
412 should be viewed as less likely to occur in nature (presuming that these campaigns could represent all
413 conditions happening in nature), but still a valuable data point drawn from a physical model that can be
414 used to bridge PO₃ with explanatory variables.



41
 416 **Figure 3.** The scatterplot comparison of simulations with observed concentrations for six unconstrained
 417 species. More than ~133,000 observations are used for HCHO, NO₂, NO, and PAN. HO_x data points are
 418 limited to ~55,000 observations. Heat maps show the density of the data. Linear fits are calculated using
 419 the ordinary least squares method.

420 4.2. Classification of aircraft data

421 Following the method described in Section 3.3, we cluster the cloud of aircraft data (~ 133k points)
 422 into seven distinct classes. We describe them using three categories: pollution level, altitude, and SZA.
 423 Figure 4 illustrates the violin plot of these classes for various chemical, solar, and meteorological
 424 conditions. Figure 5 shows their corresponding violin plot of simulated PO₃. A discussion of each class and
 425 their relationship to PO₃ follows:

426 C1 (clean, high altitude, high SZA) – Characterized by high altitude flights, cold ambient temperature, and
 427 negligible water vapor content, this class consists of observations that were typically taken during relatively
 428 high SZA with a median of 50°. While high altitude observations in clear-sky conditions often should have
 429 large photolysis rates due to reduced overhead ozone, the relatively high SZA of this class leads to low
 430 photolysis rates. FNRs tend to be large in this class due to a higher amount of HCHO over NO₂, and FNP
 431 (HCHO×NO₂) and NO₂/NO_y ratios are low due to the pristine conditions. The lack of sufficient ozone
 432 precursors and reduced photochemistry make this class undergo the lowest PO₃ rates with a median of 0.11
 433 ppbv/hr.

434 C2 (clean, high altitude, low SZA) - This category represents samples collected in low SZA conditions,
 435 resulting in the highest photolysis rates among all classes. The mass of ozone precursors and the ozone
 436 sensitivity condition are similar to those in C1. However, C2 PO₃ rates are approximately 60% higher than
 437 C1 due to increased photochemistry.

438 C3 (moderately clean, medium altitude, high SZA) - This class is characterized by observations collected
439 in mid-altitudes and high SZA. Airsheds in C3 experienced relatively more polluted air compared to C1
440 and C2 due to being closer to the surface. Photolysis rates are smaller than C1 possibly because of higher
441 ozone overhead, although we cannot rule out the varying surface albedo between the classes. Despite the
442 lower photolysis rates, C3 PO₃ (0.28 ppbv/hr) is larger than that of C2 and C1, indicating that pollution
443 levels can have a more significant impact than favorable conditions for photochemistry.

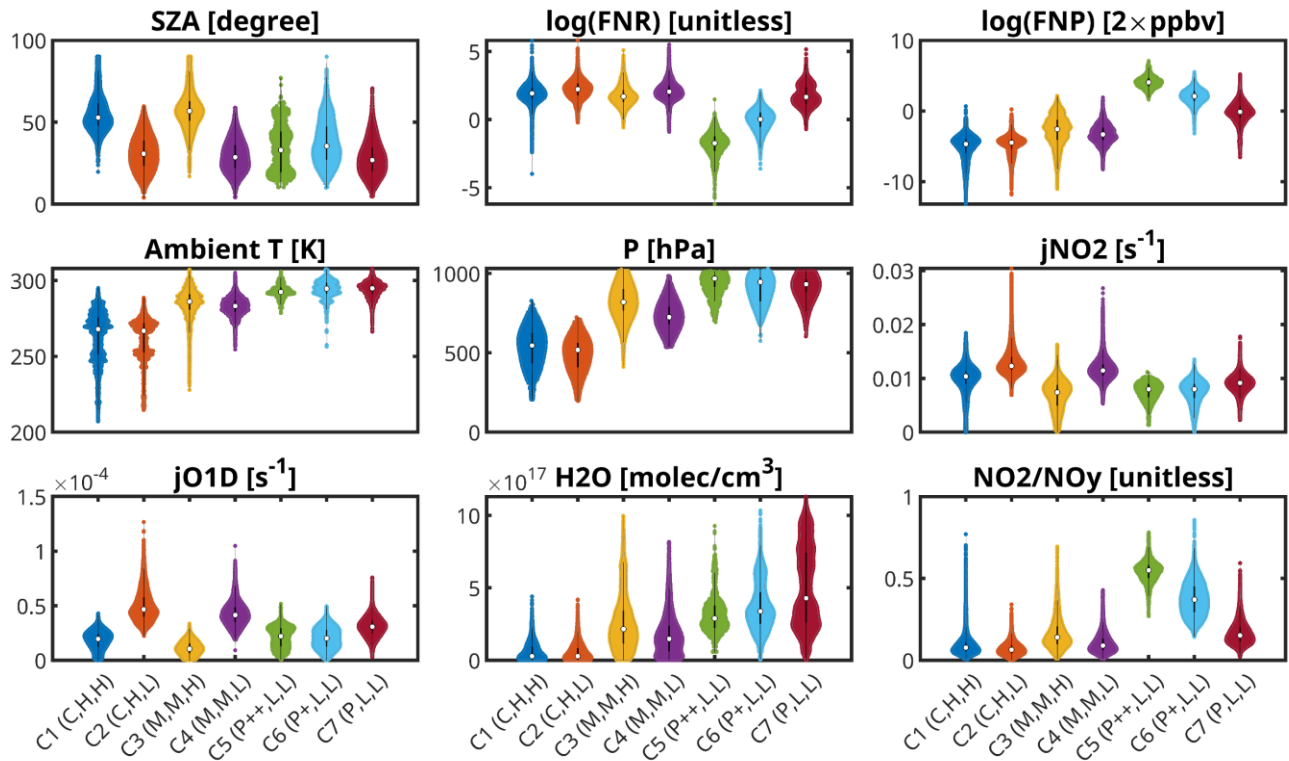
444 C4 (moderately clean, medium altitude, low SZA) - This category is distinct from C3 in terms of lower
445 SZA (resulting in more photochemistry) and a slightly smaller number of ozone precursors. As a result of
446 the lower ozone precursor concentration, not only is C4 PO₃ (0.19 ppbv/hr) lower than C3, but also is not
447 different from C2. This again implies that the amount of ozone precursors is more important than the
448 photochemistry for these conditions.

449 C5 (extremely polluted, low altitude, low SZA) - This class features the highest amount of ozone precursors
450 (median FNP ~ 58 ppbv²) among all classes. Furthermore, it is characterized by low photolysis rates due to
451 its proximity to the surface, and high NO₂/NO_y indicative of localized polluted airshed. Unlike the previous
452 classes, this class has the lowest FNR, indicating that it is mainly located in the VOC-sensitive regime. C5
453 PO₃ values are much higher than the previous classes, with a value of 3.0 ppbv/hr.

454 C6 (polluted, low altitude, low SZA) - While this class shares similar features with C5 in terms of altitude,
455 photolysis rates, and meteorology, it experiences a lower FNP (median of 8 ppbv²). Despite the lower FNP,
456 C6 has the highest amount of PO₃ (5.2 ppbv/hr) among all classes. This is a result of reduced non-linearities,
457 as this class does not often fall into an extreme VOC-sensitive regime (median FNR ~ 1.0) where nitrogen
458 oxides (NO_x) can hamper ozone production. This tendency coincides with Souri et al. (2023) which also
459 found that the highest amount of PO₃, lied between the transitional regimes, gravitated towards VOC-
460 sensitive because of abundant ozone precursors and reduced negative chemical feedback of NO_x.

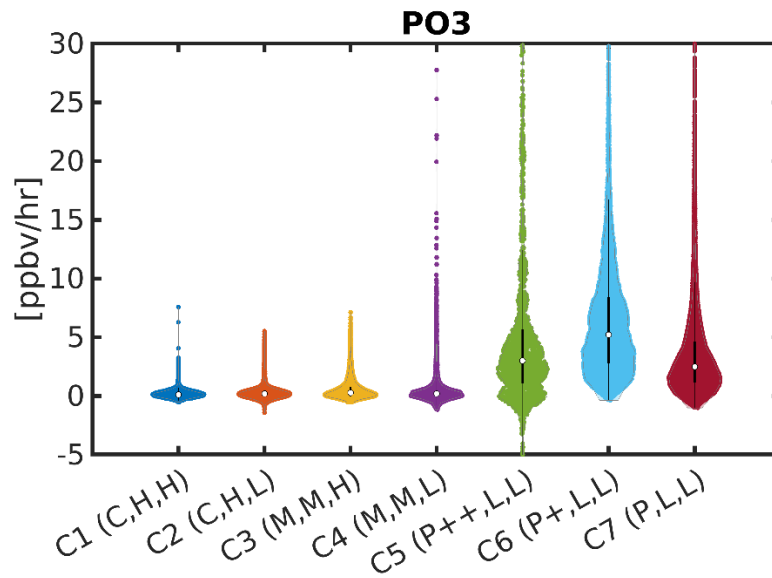
461 C7 (moderately polluted, low altitude, high SZA) - C7 is characterized by aged air close to the surface with
462 slightly higher photolysis rates than C5 and C6. C7 PO₃ is 2.5 ppbv/hr, only slightly smaller than C5 despite
463 much lower FNP (median of 0.9 ppbv²). This could be caused by the combined effect of higher photolysis
464 rates and reduced non-linear ozone chemistry.

465 The analysis of aircraft data has revealed that the levels of HCHO and NO₂, as well as the rates of
466 jNO₂ and jO¹D photolysis, play an important role in influencing PO₃. Additionally, FNRs can offer insights
467 into the sensitivity of PO₃ to its main precursors. These findings align with numerous other studies that
468 have examined the factors driving PO₃ (e.g., Duncan and Chameides, 1998; Thornton et al., 2002; Kleiman
469 et al., 2002; Gerasopoulos et al., 2006; Chatfield et al., 2010; Baylon et al., 2018; Wang et al., 2020; Souri
470 et al., 2023). Consequently, our PO₃ estimates will incorporate HCHO, NO₂, jNO₂, jO¹D, and FNR. While
471 the cluster analysis did not definitively indicate whether meteorological conditions impact PO₃, we will
472 also include ambient temperature, water vapor, pressure, and SZA to determine if they provide any
473 additional insights into PO₃ estimates.



474

475 **Figure 4.** The violin plots of six different parameters coming from the box model clustered into seven
 476 distinct categories. Each cluster is described by three labels: air pollution levels (C: clean, M: moderately
 477 clean, P: moderately polluted, P+: polluted, P++: extremely polluted), altitude (H: high, M: medium, L:
 478 low), and SZA (H: high, L: low). The white dot is the median and the bars explain the 75th and 25th
 479 percentiles. Both FNR and FNP are scaled using the logarithmic function to enable the simultaneous
 480 visualization of low and high values within a single plot.



481

482 **Figure 5.** The corresponding violin plots of simulated PO_3 for the seven clusters described in Figure 4.
 483 The lowest PO_3 is seen in remote regions (C-M) where ozone precursors are minimal. The highest PO_3
 484 does not happen in the most polluted region (P++) resulting from the non-linear ozone chemistry.

485 4.3. Estimates of PO_3

486 4.3.1. LASSO coefficients

487 Armed with a procedure that finds the important features in a linear model (Section 3.1), we now
 488 explore using LASSO for PO_3 estimation. We make use of all data points generated by the observationally-
 489 constrained box model from various atmospheric composition campaigns. Among the selected variables
 490 shown in Figure 2, the LASSO algorithm assigns zero coefficients to SZA, pressure, temperature, and water
 491 vapor, indicating that they offer less valuable information compared to other variables. This decision was
 492 made by systematically adjusting the regularization factor within a 10-fold cross-validation framework to
 493 identify the optimal factor that strikes a balance between solution variance and prediction bias. As a result,
 494 the LASSO algorithm suggests that HCHO, NO_2 , jNO_2 , and JO^1D contain sufficient information to
 495 accurately predict PO_3 for the most part.

496 Table 1 provides the intercepts and the corresponding coefficients for four different regions
 497 separated by FNR. While we do not expect for a statistical model to fully single out the “cause and effect”
 498 relationship between explanatory variables and the target, we note that it has some basic understanding of
 499 ozone chemistry; the HCHO coefficients increase as moving towards smaller FNRs (i.e., more VOC-
 500 sensitive). The same tendency is evident with respect to NO_2 and larger FNRs (i.e., more NO_x -sensitive).
 501 The negative coefficient of NO_2 in regions having $\text{FNR} \leq 1.5$, implies some levels of non-linear feedback
 502 embedded in this parameterization. Both jNO_2 and JO^1D have positive coefficients throughout the chemical
 503 conditions, suggesting that higher photolysis rates accelerate PO_3 . JO^1D has a smaller effect than jNO_2 on
 504 PO_3 over remote regions ($\text{FNR} \geq 3.5$) perhaps because of redundant information available compared to jNO_2 .

505 **Table 1.** Calibrated coefficients derived from the LASSO estimator using seven atmospheric
 506 composition aircraft campaigns.

Group	Criteria for FNR	Intercept	HCHO [ppbv]	NO_2 [ppbv]	$\text{jNO}_2 \times 10^3$ [s^{-1}]	$\text{JO}^1\text{D} \times 10^6$ [s^{-1}]
1	$\text{FNR} \leq 1.5$	-1.98	1.85	-0.14	0.12	0.09
2	$1.5 < \text{FNR} < 2.5$	-3.38	1.79	0.98	0.19	0.07
3	$2.5 < \text{FNR} < 3.5$	-3.27	1.07	3.48	0.21	0.03
4	$\text{FNR} \geq 3.5$	-1.63	0.41	6.54	0.11	0.01

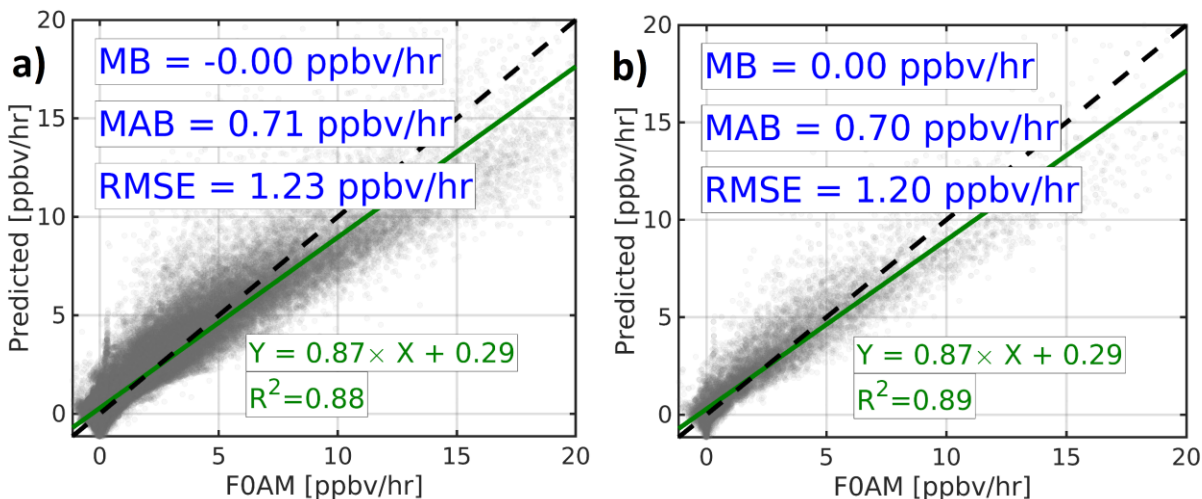
507

508 4.3.2. Validation of PO_3 predictions

509 The validation of PO_3 prediction against the box model results is performed in threefold with an
 510 increasing stringency order: i) using all data points used in the LASSO algorithm, ii) by randomly dropping
 511 data points, and iii) by dropping each air quality campaign from the LASSO estimation and using its data
 512 as benchmark.

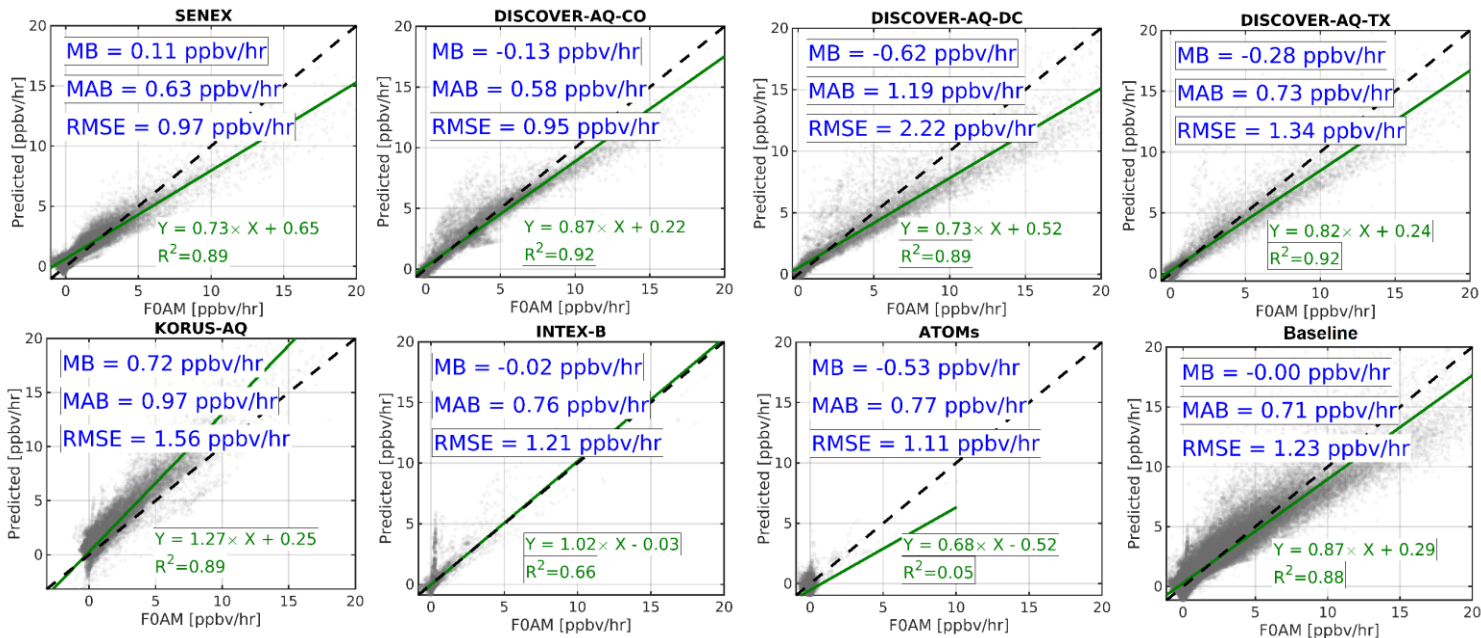
513 Figure 6a shows the scatterplot of predicted PO_3 against the box model for all data points used to
 514 estimate the coefficients described in Section 4.3.1. Despite the algorithm's simplicity, we can recreate more
 515 than 88% of the variance in PO_3 with negligible absolute bias. This has an important indication that our
 516 scientific problem is not overly complex. There is less than 30% bias with respect to the mean absolute bias
 517 of the prediction. The positive offset and a slope smaller than one indicate a mild underestimation
 518 (overestimation) of PO_3 in polluted (clean) regions. Figure 6b shows the same analysis for 20,000 randomly
 519 chosen data points (~15% of the total) that we purposefully dropped from the LASSO estimation to gauge
 520 if the predictor model can replicate numbers for points not used during the training. We find almost identical
 521 statistics for these points, suggesting that the prediction stays robust for points outside the training data set.

522 However, the most stringent method is to drop each campaign data set entirely to understand where the
523 prediction model struggles most.



524
525 **Figure 6.** Scatterplots comparing observationally-constrained FOAM model PO_3 and the predictions based
526 on the proposed algorithm for (a) all data points and (b) 20,000 randomly-dropped data points as
527 benchmarks. Despite the simplicity of the algorithm, we can reproduce a large variance in PO_3 using only
528 four explanatory variables.

529 Figure 7 shows several subplots pertaining to dropped campaigns from the analysis. Immediately
530 evident is that our PO_3 estimation has considerable skills at capturing PO_3 for most polluted cases, including
531 DISCOVER-AQs, KORUS-AQ, and SENEX without using their individual datasets. This provides
532 convincing evidence about a high degree of generalizability of the predictor. However, the model has a
533 reduction in performance in INTEX-B for $PO_3 < 1$ ppbv/h. Moreover, the model prediction power is
534 consistently poor for ATOMs where a significant fraction of airsheds were samples in pristine areas. We see
535 such poor performance for $PO_3 < 1$ ppbv/hr for other campaigns such as KORUS-AQ. Therefore, it is
536 difficult to have confidence in the predictive power of the model in remote regions, which may be caused
537 by the lack of inclusion of HOx, halogens, and H_2O in the fit, as they can become an important sink for
538 tropospheric ozone in those areas (Simpson et al., 2015). Nonetheless, while our predictive accuracy
539 remains poor for this specific subset of the data, the practical utility and significance of this specific region
540 (i.e., pristine areas) for air quality applications are notably limited. Given these results, we limit our
541 predictions to $PO_3 > 1$ ppbv/hr for the subsequent analyses.



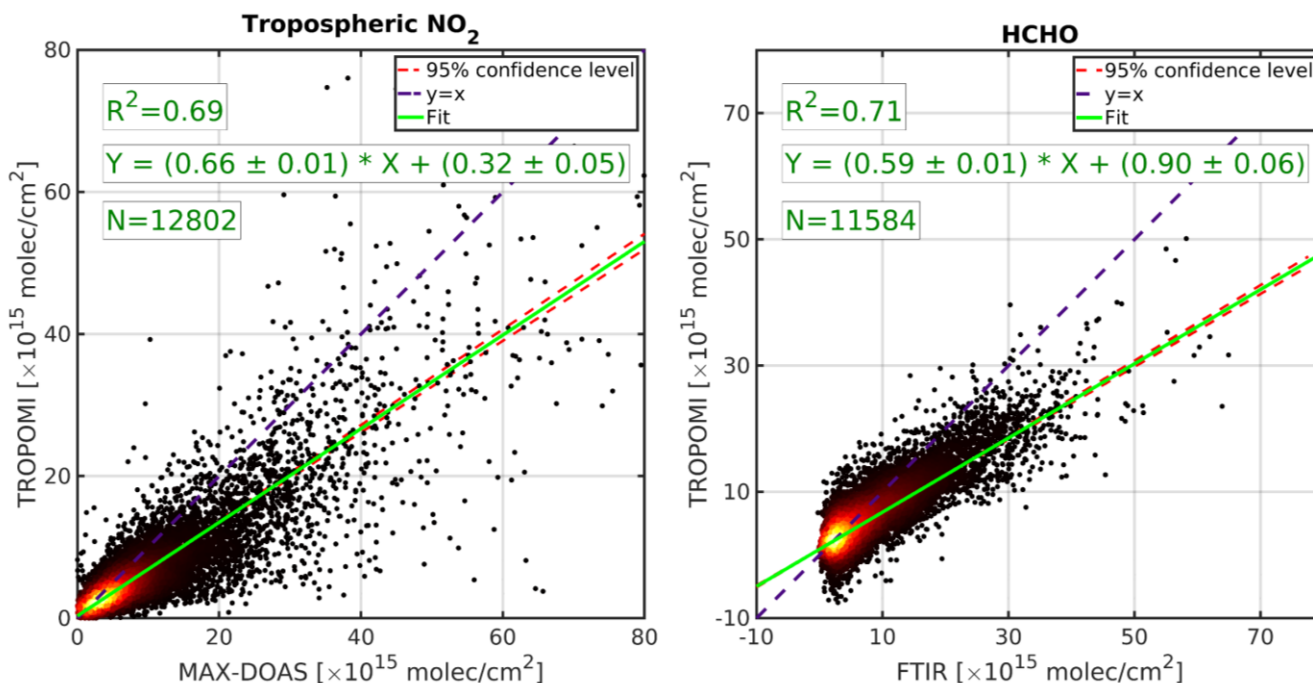
543 **Figure 7.** Same as Figure 6b, but each campaign is dropped from the LASSO estimation and subsequently
 544 used as an independent benchmark. The designed algorithm has shown a high degree of skill at predicting
 545 PO_3 in polluted regions; however, it performs poorly in pristine areas.

546 4.3.3. TROPOMI NO_2 and HCHO validation

547 To build confidence in our quantitative application of TROPOMI data for PO_3 estimates, we
 548 validate the daily tropospheric NO_2 and total HCHO columns against MAX-DOAS and FTIR observations
 549 based upon the validation framework outlined in Vigouroux et al. (2020) and Verheolst et al. (2021). Both
 550 paired datasets have been expanded to late 2023 showing a fuller picture of TROPOMI error
 551 characterization compared to former studies. Figure 8 shows the comparison of daily TROPOMI, the
 552 benchmarks and the optimal fit associated with their errors for the period of 2018-2023.

553 In the context of tropospheric NO_2 comparison, we observe a slope smaller than one (~ 0.66) with
 554 a positive offset ($0.32 \times 10^{15} \text{ molec/cm}^2$). This tendency has been repeatedly documented in various studies
 555 for various satellites or benchmarks (e.g., Griffin et al., 2019; Choi et al., 2020; Verhoelst et al. 2021; van
 556 Geffen et al., 2022). A slope smaller than one, originating from unresolved systematic biases, implies that
 557 TROPOMI is biased-low in polluted regions. A slight positive offset suggests that TROPOMI NO_2 is
 558 biased-high in remote regions. The errors of slope and the offset are relatively small, evidence of the
 559 robustness of the optimal fit against the dataset variance. Nonetheless, we will incorporate them into Eqs 2
 560 and 3 to take the adjustment error into consideration.

561 Despite the inherent difficulty in obtaining HCHO observations from the UV-Vis imagery
 562 (González Abad et al., 2019), the HCHO comparison exhibits a good alignment with benchmarks. Like the
 563 previous comparison, the slope is smaller than one (~ 0.59) and the offset is positive ($\sim 0.9 \times 10^{15} \text{ molec/cm}^2$)
 564 agreeing within 10% with studies done by Vigouroux et al. (2020) and De Smedt et al. (2021).
 565 Consequently, we will consider the fit errors and adjust all VCDs based on the slope and the offset obtained
 566 from this comparison.



567

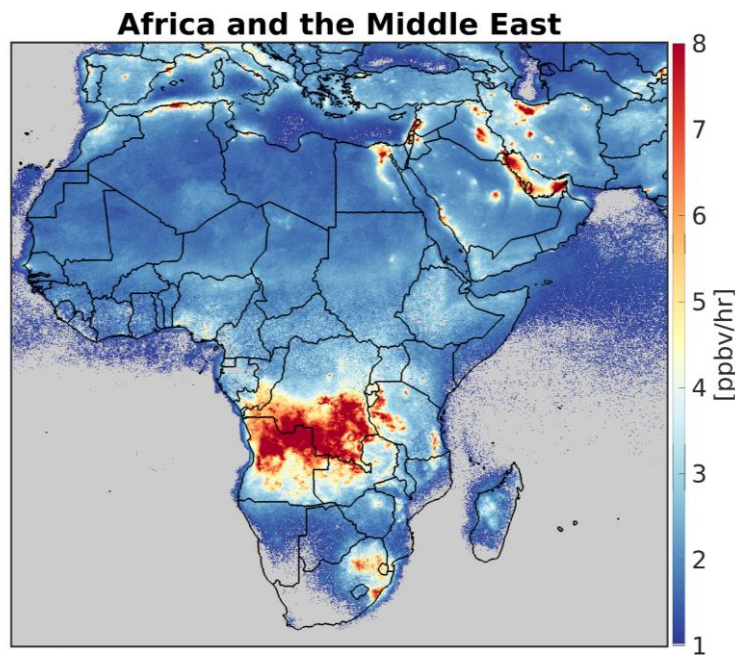
568 **Figure 8.** The comparison of TROPOMI tropospheric NO₂ and MAX-DOAS (left) and TROPOMI HCHO
 569 and FTIR (right). The data points cover the period of 2018-2023. Both errors of in-situ measurements and
 570 TROPOMI are considered in the fit. The data curation procedure has been discussed in Verhoelst et al.
 571 (2021) and Vigouroux et al. (2020). The slope smaller than one suggests that both HCHO and NO₂ retrievals
 572 are underestimated in polluted regions.

573 4.3.4. Maps of PO₃ across various regions and qualitative description

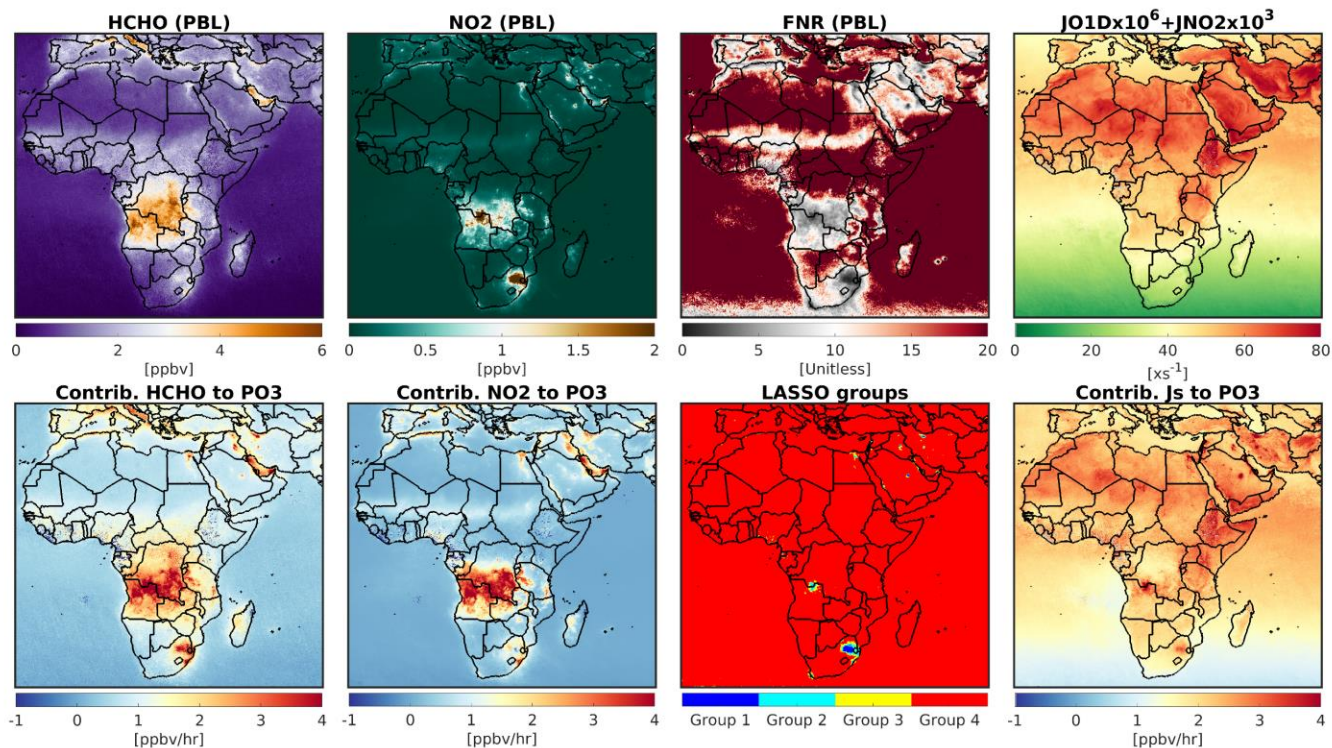
574 Taking advantage of the wealth of bias-corrected TROPOMI observations, we present the first-ever
 575 reported PO₃ maps at 0.1×0.1 degrees in the PBL in July 2019 across various geographic regions. Moreover,
 576 because of the explicit nature of our algorithm, it is straightforward to break down the contributors of PO₃
 577 to gather insights into how each driver has shaped the distribution of PO₃. Therefore, in addition to PO₃
 578 maps, we will show the magnitudes of various drivers of PO₃ including NO₂, HCHO, and FNR
 579 concentrations in the PBL region, the sum of scaled jO¹D and jNO₂ values, along with their contributions
 580 to PO₃. It is worth noting that these maps are only a snapshot of PO₃ whose precursors can have large
 581 interannual and interdecadal variability caused by meteorology, chemistry, and emissions. A discussion on
 582 each region follows:

583 *Africa and the Middle East* – Figure 9 illustrates the accelerated rates of PO₃ over the region, particularly
 584 concentrated over major cities such as Tehran (Iran), Cairo (Egypt), Riyadh (Saudi), Baghdad (Iraq), Algiers
 585 (Algeria), and Johannesburg (South Africa). These urban areas consistently experience poor air quality
 586 episodes (e.g., Chaichan et al., 2016; Belhout et al., 2018; Yousefian et al., 2020; Thompson et al., 2014;
 587 Boraiy et al., 2023; Choi and Sourì et al. 2015a). The biomass burning activities in Africa (see Figure 1 in
 588 Roberts et al., 2009) significantly contribute to the high rates of PO₃. Moreover, we see accelerated PO₃
 589 over the Persian Gulf, a region housing oil and gas production facilities, leading to high PO₃ in the region
 590 (Lelieveld et al., 2009; Choi and Sourì et al. 2015a). Figure 10 shows NO₂ and HCHO concentrations are
 591 highly correlated in the Middle East ($r=0.82$) due to co-emitted NO_x and VOC emissions, predominantly
 592 from anthropogenic sources. Over the whole region, HCHO and NO₂ concentrations are only moderately
 593 correlated ($r=0.61$). This is because there is strong spatial heterogeneity associated with NO_x and VOC
 594 emissions over Africa that are not spatially correlated. One possible explanation for this could be the
 595 emission dependence on the type of fire combustion in Africa (van der Velde et al., 2021) and the location

596 of biogenic isoprene emissions (Marais et al., 2014). For the most part, FNRs tend to fall in ranges above
597 >3.5 (LASSO group 4, highly NO_x-sensitive). However, lower FNRs are prevalent in the core of cities due
598 to elevated NO_x emissions. The contributions of HCHO to PO₃ occur predominantly over areas with low
599 FNRs. These results suggest that NO_x emissions dictate the location of maximum VOC contributions to
600 PO₃. The contribution of NO₂ to PO₃ behaves non-linearly with negative values at the core of cities such as
601 Johannesburg and Tehran (Figure S2). Photolysis rates are high over low SZA and bright surface albedo
602 (i.e., arid land). Accordingly, photolysis rates exhibit a latitudinal gradient in response to changes in SZA.
603 Greater contributions of photolysis rates to PO₃ are observed in areas with low FNRs, as determined by the
604 LASSO estimator (Table 1).



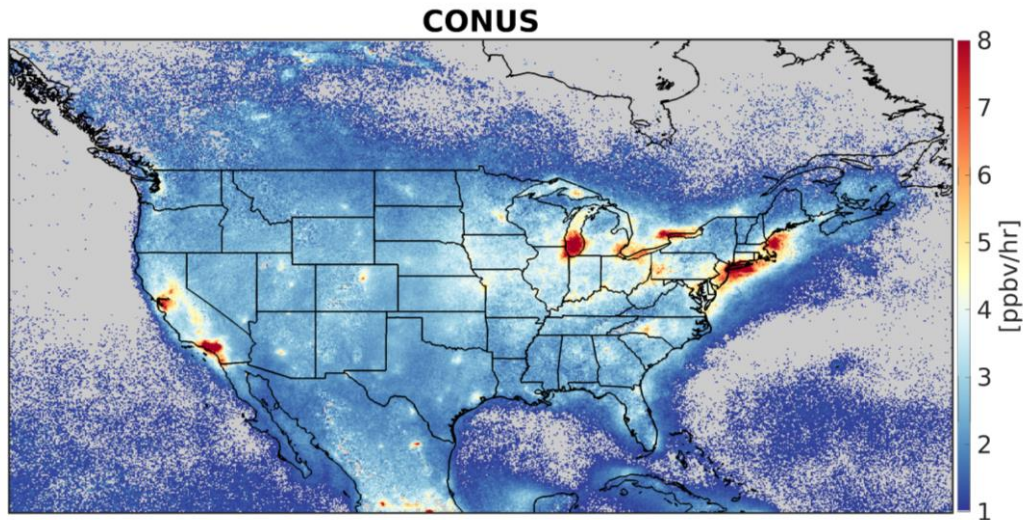
605
606 **Figure 9.** The spatial distribution of PO₃ within the PBL region averaged over July 2019 in Africa and the
607 Middle East. PO₃<1 ppbv/hr is masked due to the algorithm deficiencies. Accelerated PO₃ can be seen over
608 major cities and biomass burning activities in Africa.



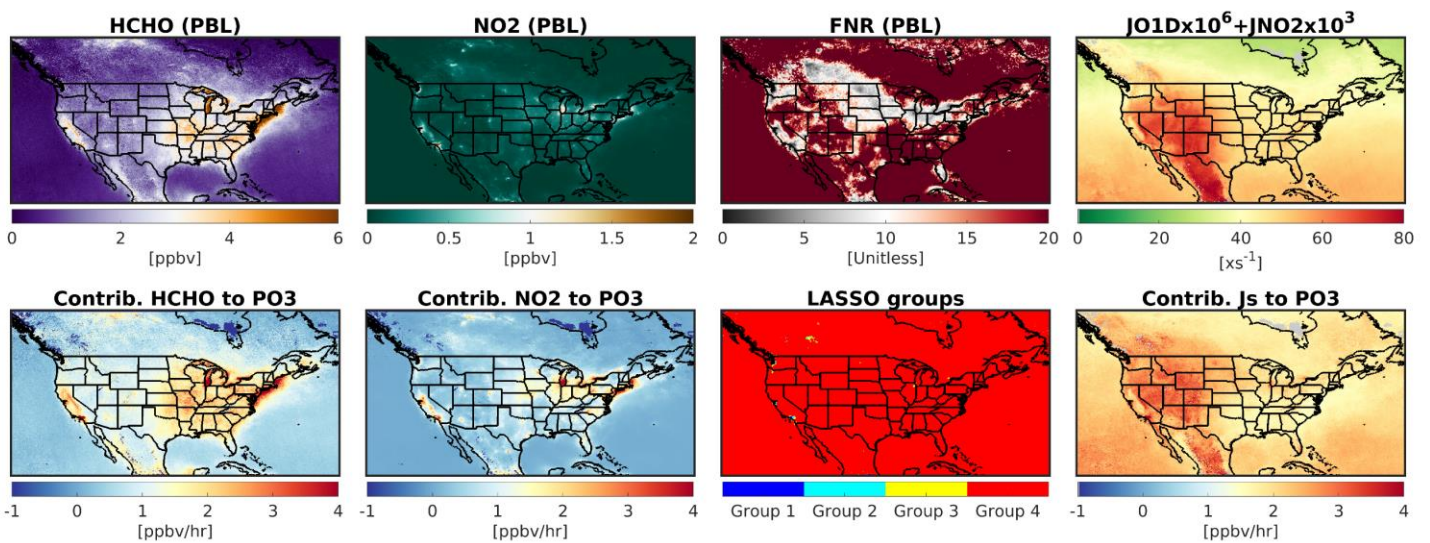
609

610 **Figure 10.** (first row) PBL concentrations of HCHO, NO₂, FNR and sum of scaled jO¹D and jNO₂ derived
 611 from TROPOMI and models in July 2019; (second row) the contributions of HCHO, NO₂, and photolysis
 612 rates to PO₃, along with the defined LASSO ozone production sensitivity regimes for PO₃ estimates.

613 *Contiguous United States (CONUS)* – New York City, Los Angeles (LA), the San Francisco Bay area, and
 614 Lake Michigan areas all experience accelerated PO₃ in July 2019, as shown in Figure 11. All the regions
 615 fall into non-attainment regions (marginal to extreme) with respect to ozone standards and have been
 616 immensely studied (Wu et al., 2024; Kim et al., 2022; Stainer et al., 2021). A robust relationship between
 617 PO₃ and ozone concentrations can only be established by factoring in physical processes such as horizontal
 618 and vertical transport, dry deposition rates, and background values. In regions with high background ozone
 619 concentrations, for example in mountainous areas, even a moderate level of PO₃ can elevate ozone
 620 concentration to unhealthy levels. Conversely, if there is a strong correlation between PO₃ and frequent
 621 ozone exceedances, such as those observed in the mentioned U.S. cities, it indicates that locally produced
 622 ozone through chemical reactions is the primary factor contributing to those events. Except for LA, the vast
 623 majority of CONUS fall into large FNRs (>3.5), meaning NO₂ levels largely shape the spatial distribution
 624 of PO₃ (Figure 12). HCHO levels are found to be relatively large over LA, causing PO₃ to increase due to
 625 its greater sensitivity to VOCs. In addition to high levels of HCHO and NO₂ in several Californian regions,
 626 accelerated photochemistry caused by the bright surface albedo enhances PO₃.

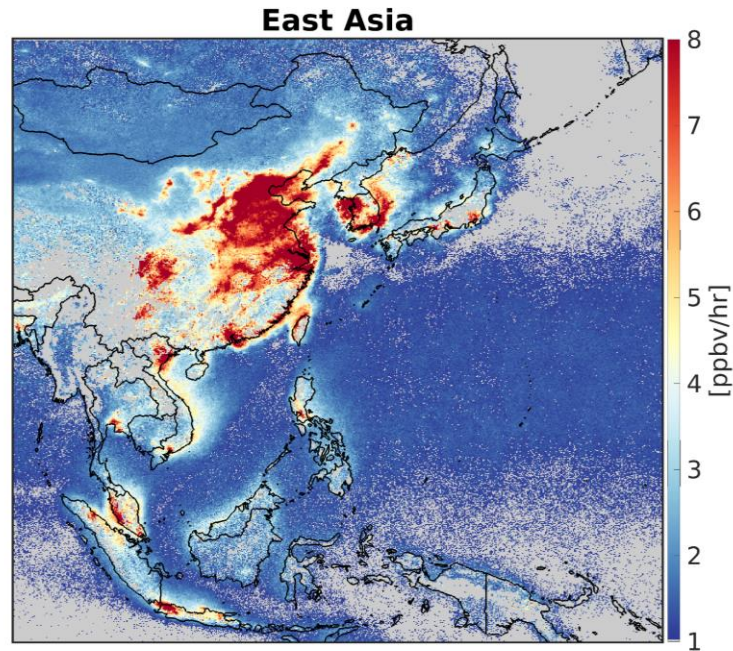


627
 628 **Figure 11.** Same as Figure 9 but for CONUS. Elevated PO₃ prevails over various areas such as New York
 629 City, Los Angeles, San Francisco Bay area, and Lake Michigan.



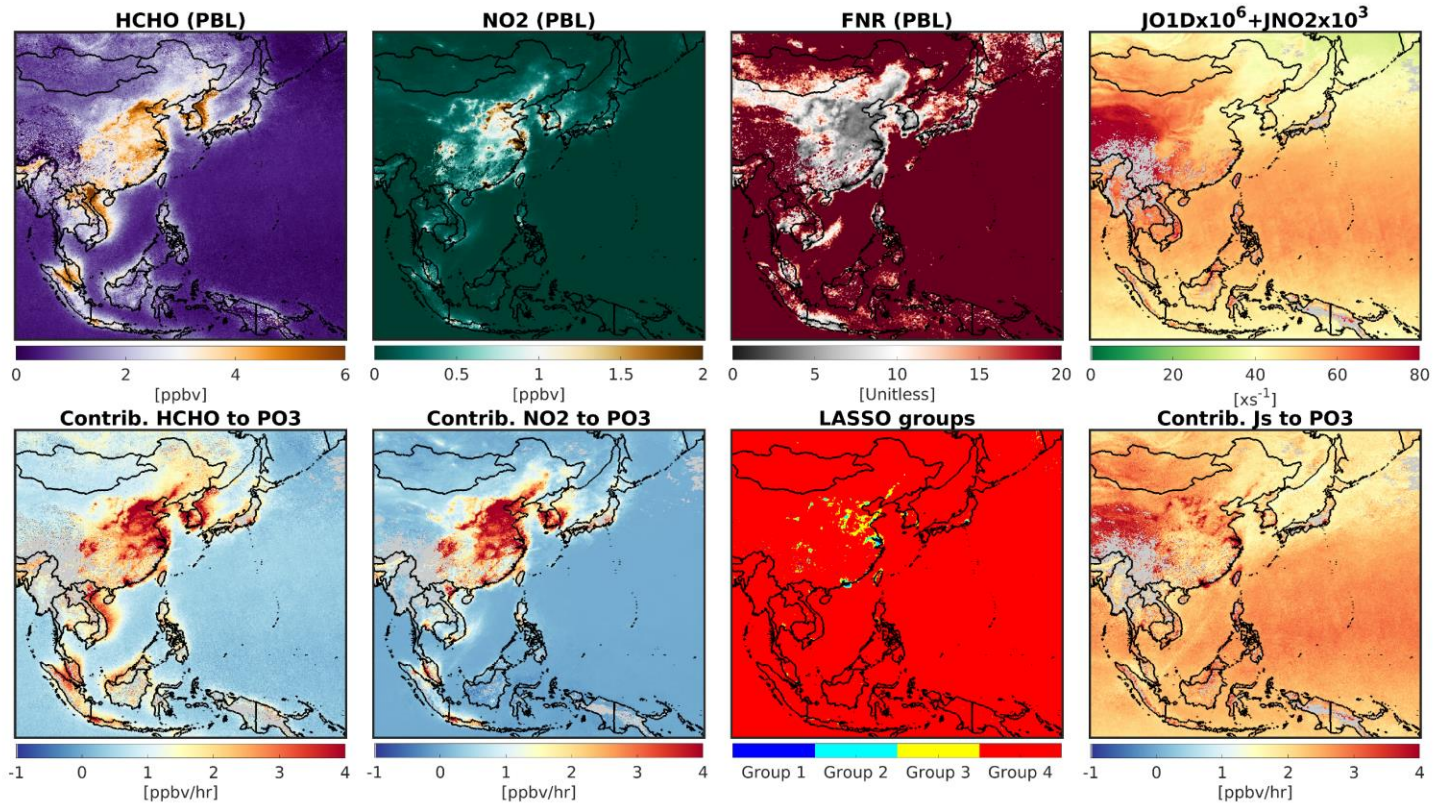
631 **Figure 12.** Same as Figure 10 but for CONUS.

632 *East and Southeast Asia* – Figure 13 shows extremely accelerated PO₃ values over East Asia, particularly
 633 over North China Plain, Yangtze River Delta, Pearl River Delta, and Seoul. These regions have experienced
 634 severely degraded air quality with respect to ozone (Souri et al., 2020a,b; Li et al., 2019; Colombi et al.,
 635 2023; Schroeder et al., 2020; Wang et al., 2017; Zhang et al., 2007). In southeast Asia, Hanoi (Vietnam),
 636 Kuala Lumpur (Malaysia), and Jakarta (Indonesia), undergoing heightened PO₃ as well, have received less
 637 attention in literature (Ahamad et al., 2020; Kusumaningtyas et al., 2024; Sakamoto et al., 2018). Figure 14
 638 suggests that the chemical condition of many regions in China and South Korea, falling within the
 639 transitional regimes (LASSO group 2 and 3, 1.5 < FNR < 3.5), has made them susceptible to high PO₃ levels
 640 due to concurrent high concentrations of HCHO and NO₂. Moreover, photochemistry appears to be active
 641 throughout the region.



642

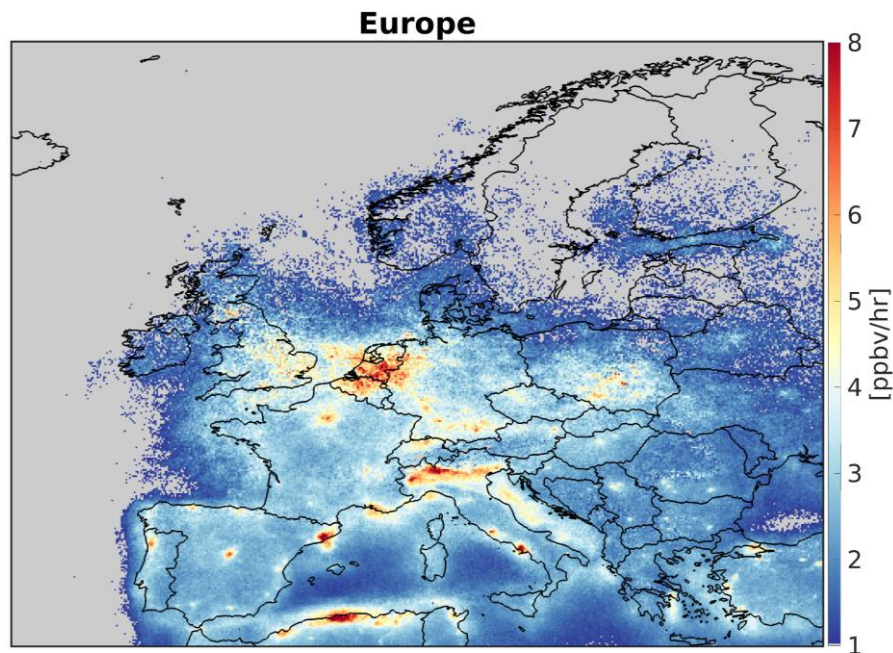
643 **Figure 13.** Same as Figure 9 but for east and southeast Asia. Because of heightened amount of
 644 photochemistry, NO_2 , and HCHO, we observe accelerated PO_3 throughout the majority of the cities in East
 645 and Southeast Asia.



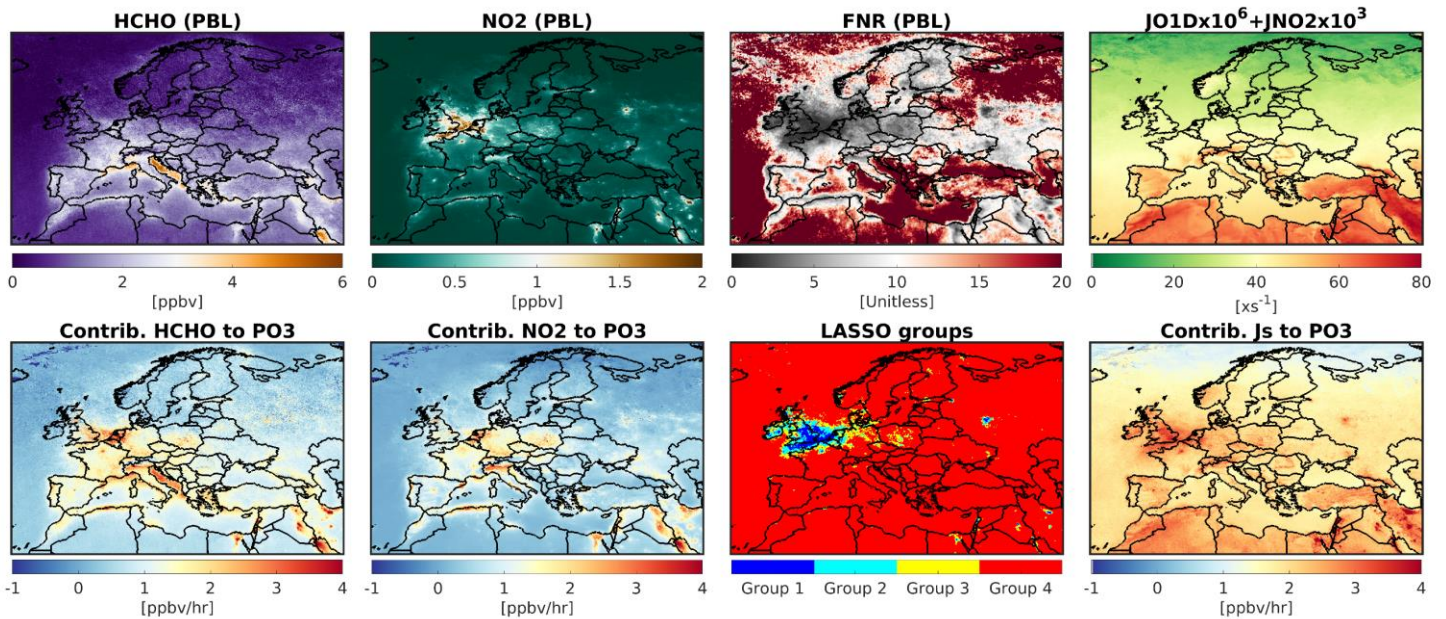
6

647 **Figure 14.** Same as Figure 10 but for east and southeast Asia.

648 *Europe* – Figure 15 reveals high PO_3 over Benelux (Belgium, The Netherlands, and Luxembourg), Po
649 Valley (Italy), and several major cities such as Barcelona (Spain) and Rome (Italy). Benelux has the largest
650 hotspot of PO_3 in the region (e.g., Zara et al., 2021). A significant portion of England, Benelux, fall into
651 VOC-sensitive, or the transitional regime ($\text{FNR} < 2.5$) shown in Figure 16. Because of diminished
652 photochemistry in these high latitude regions, we do not see significant PBL concentrations of HCHO in
653 order for PO_3 to be as high as the previous areas; moreover, the non-linear NO_x feedback has led to negative
654 contributions of NO_2 to PO_3 in several cities such as London. In general, low photolysis rates compared to
655 the previous regions have made most of Europe less prone to elevated PO_3 .



656
657 **Figure 15.** Same as Figure 9 but for Europe. Because of reduced photochemistry, PO_3 values tend to be
658 smaller than the previous cases. Benelux has experienced the highest PO_3 in this region.



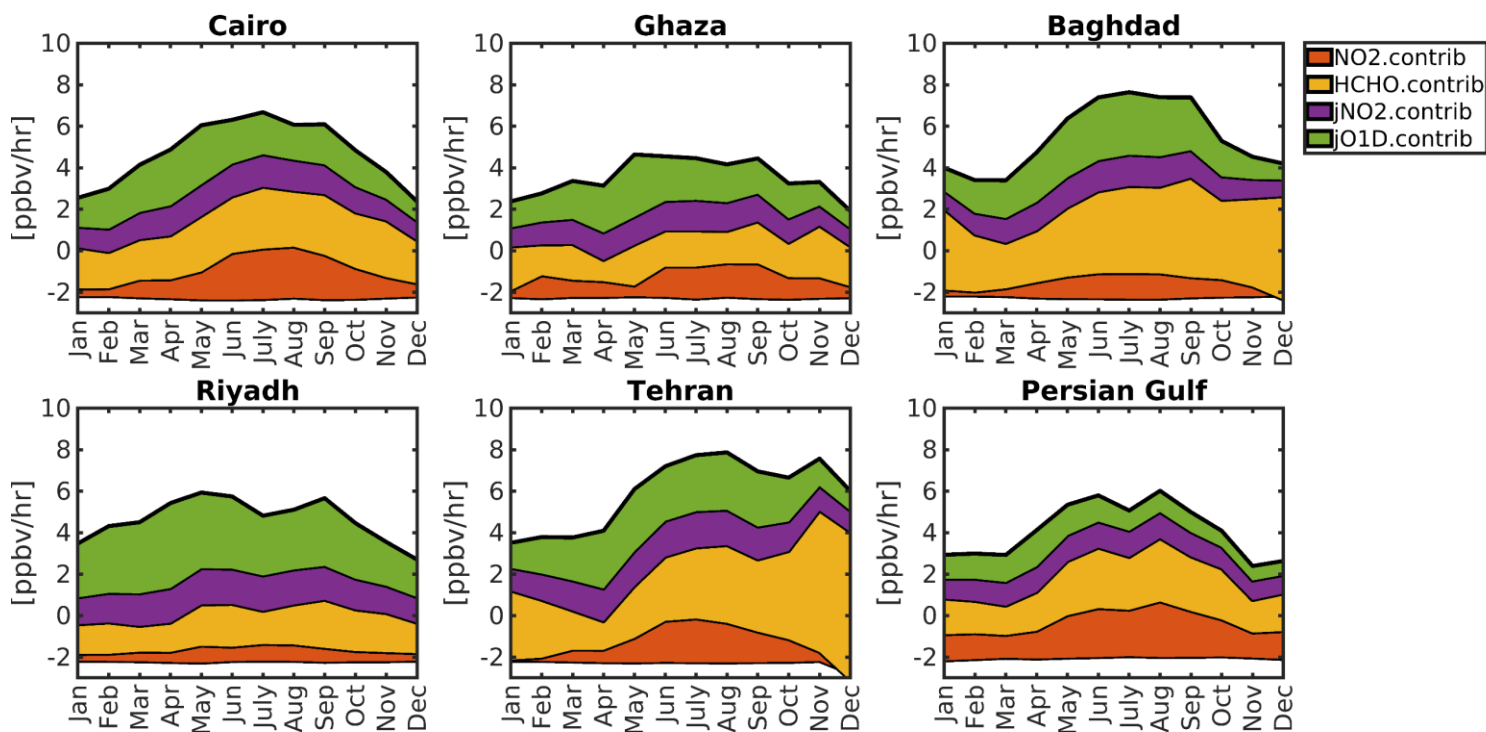
€

660 **Figure 16.** Same as Figure 10 but for Europe.

661 *4.3.5. Seasonality of PO₃ over the Middle East*

662 It is attractive to study the seasonal variations in the contributors to PO₃ over several major cities
 663 because the PO₃ drivers' seasonality can vary from location to location. We decide to focus on several
 664 Middle Eastern countries that have experienced rapid growth and degraded air quality: Cairo (Egypt),
 665 Ghaza (Palestine), Baghdad (Iraq), Riyadh (Saudi Arabia), Tehran (Iran), and the Persian Gulf region. We
 666 illustrate the seasonality of four major contributors to PO₃ including NO₂, HCHO, jNO₂, and jO¹D in 2019
 667 in Figure 17.

668 The levels of HCHO (a proxy for VOCs) consistently have the greatest impact on PO₃ throughout
 669 the year in these regions. Specifically, both Baghdad and Tehran experience high levels of HCHO even
 670 during colder months, which can be observed using TROPOMI. This suggests that regulations targeting the
 671 reduction of man-made VOC emissions should be prioritized in this region. PO₃ levels over Cairo, Gaza,
 672 Baghdad, and the Persian Gulf peak during summertime, while Tehran experiences a comparable peak in
 673 the autumn due to increased VOC emissions. Additionally, we notice a decrease in PO₃ levels over the
 674 Persian Gulf and Riyadh in July, possibly due to a decline in HCHO contributions caused by meteorological
 675 factors. Even though NO₂ concentrations decline in summertime due to shorter lifetime against OH, the
 676 higher amount of HCHO makes PO₃ more sensitive to NO₂ in this season. Ghaza shows the least seasonal
 677 variation among these regions, likely due to consistently active photochemistry throughout the year.

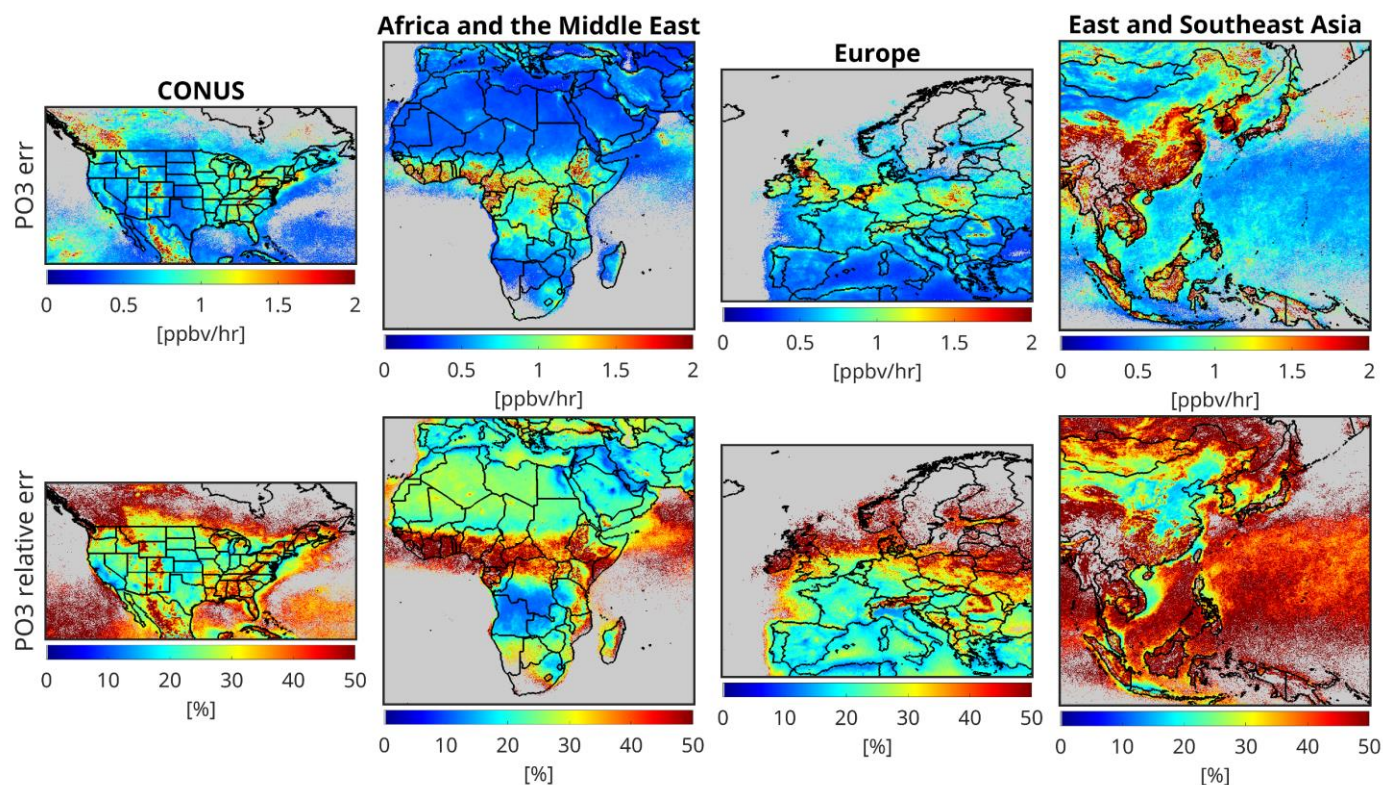


679 **Figure 17.** The contributions of NO₂, HCHO, jNO₂, and jO¹D to the PBL PO₃ for several major regions in
 680 the Middle East. These estimates are based on the proposed algorithm integrating TROPOMI, ground-based
 681 remote sensing, and atmospheric models, to estimate PO₃ based upon a statistical approach. PO₃ tends to
 682 spike around the summer due to increased HCHO, higher sensitivity of PO₃ to NO_x, and enhanced
 683 photochemistry. However, Tehran shows a second peak in autumn due to unusual high values of HCHO.

684 *4.3.6. The effect of satellite errors on PO₃*

685 Satellite retrieval errors have been identified as the primary obstacle to achieving a robust
 686 understanding of ozone chemistry using HCHO and NO₂ data (Souri et al., 2023; Johnson et al., 2023);
 687 therefore, generating uncertainty maps is crucial for informing the scientific community about the
 688 credibility of our PO₃ estimates. In this study, we utilize the equations outlined in Section 2.2.1 to propagate
 689 the errors of HCHO and NO₂ retrievals to the final PO₃ estimates. We achieve this by recalculating the PO₃
 690 value for a given pixel 10,000 times, with each recalculation based on a sample drawn from a normal
 691 distribution with a standard deviation equal to the satellite total error. The standard deviation of these
 692 samples offers a good approximation of the impact of satellite errors on PO₃ estimates.

693 Figure 18 illustrates the maps of PO₃ absolute and relative errors over the targeted regions in the
 694 course of the month of July. The errors of PO₃ estimates tend to be high (> 50%) in remote regions where
 695 the trace gas signals are small. However, the PO₃ errors are within 10-20% in polluted regions where the
 696 signals are larger. Currently, the absence of absolute measurements of PO₃ at this vast spatial coverage
 697 makes it challenging to judge the severity of these errors for PO₃ applications. Nonetheless, any application
 698 based on this product should be recalculated within the reported errors through a Monte-Carlo to gauge the
 699 significance of the outcome.



701 **Figure 18.** The influence of the satellite errors on PO_3 estimates (absolute and relative) over four major
 702 regions tackled in this work. The errors are based on monthly-averaged TROPOMI errors. The errors tend
 703 to be mild over polluted regions (10-20%) but they can exceed above 50% over pristine ones.

704 **5. Conclusion**

705 Providing data-driven and integrated maps of ozone production rates (PO_3) using a synergy of
 706 satellite retrievals, ground-based remote sensing, and atmospheric models enabled us to generate the first
 707 satellite-informed product of this kind, offering extensive spatial coverage with important applications in
 708 atmospheric chemistry. These data have indeed extended the use of formaldehyde (HCHO) over nitrogen
 709 dioxide (NO_2) ratios (FNR) beyond their current role. Through this product, we can shed light on the effects
 710 of emission regulations, wildfires, widespread lockdown, wars, and economic recessions on PO_3 levels.
 711 Furthermore, given the long-term records of satellite observations (e.g., OMI since 2005 and TROPOMI
 712 since 2018), this product can inform emission regulators about locally-produced ozone hotspots, and
 713 ultimately, enhance our understanding of the spatiotemporal variability of ozone formation for over two
 714 decades.

715 In this study, we generated PO_3 maps within the planetary boundary layer (PBL), constrained by
 716 bias-corrected TROPospheric Monitoring Instrument (TROPOMI) observations, using a piecewise
 717 regularized regression model. This model was calibrated using a blend of data from a comprehensive suite
 718 of aircraft observations and a well-characterized box model. These maps, produced for various regions,
 719 allowed us to identify hotspots of locally-produced ozone pollution with unprecedented resolution. Our
 720 findings indicated that numerous urban areas in the Middle East, East Asia, and Southeast Asia exhibit
 721 accelerated PO_3 rates (>8 ppbv/hr), attributed to high levels of anthropogenic nitrogen oxides ($\text{NO}_x = \text{NO}$
 722 + NO_2), volatile organic compounds (VOCs), and active photochemistry. In contrast, such elevated PO_3
 723 levels were less prevalent in the United States and Europe, with exceptions including Los Angeles, New

724 York City, and the entire region of the Benelux. Additionally, biomass burning activities in Africa
725 contributed to high PO_3 rates across extensive areas. Seasonality of PO_3 peaked around the summer for
726 several regions in the Middle East because of active photochemistry and concurrent large HCHO and NO_2
727 levels; however, Tehran experienced elevated PO_3 in the autumn due to large HCHO values possibly
728 produced from anthropogenic emissions.

729 The production of these maps relied heavily on a robust training dataset. To this end, we
730 incorporated an extensive array of aircraft observations from multiple atmospheric composition campaigns,
731 including DISCOVER-AQ, KORUS-AQ, INTEX-B, ATOM, and SENEX, into the Framework for 0-D
732 Atmospheric Modeling (FOAM) photochemical box model. The box model demonstrated a high level of
733 correspondence ($R^2 > 0.6$, with minimal biases) between several unconstrained compounds (e.g., HCHO,
734 OH, HO_2 , PAN, NO, and NO_2) and their observed counterparts, indicating its effectiveness in understanding
735 local ozone chemistry. Utilizing a classification algorithm applied to the data obtained from the constrained
736 box model, we identified HCHO, NO_2 , their ratio (known as FNR), photolysis rates, and, to some extent,
737 meteorological factors as good candidates for reproducing PO_3 variability and magnitudes.

738 Subsequently, we employed a piecewise linear model known as LASSO, which is capable of
739 feature selection by eliminating unimportant inputs, to parameterize PO_3 . A key component of this
740 parameterization was the use of FNR to empirically linearize the non-linear ozone chemistry. The LASSO
741 algorithm indicated that more than 88% of the variance in PO_3 could be reproduced with low bias using
742 only five parameters: FNR, HCHO, NO_2 , $j\text{NO}_2$ (photolysis rates for $\text{NO}_2 + hv$), and $j\text{O}^1\text{D}$ (photolysis rates
743 for $\text{O}_3 + hv$). This parameterization demonstrated remarkable performance for the majority of air parcels
744 collected in moderately to extremely polluted regions ($\text{PO}_3 > 1$ ppbv/hr). However, it performed poorly in
745 pristine regions due to the exclusion of certain ozone loss pathways, such as HO_x ($\text{OH} + \text{HO}_2$), which are
746 more challenging to predict.

747 Fortunately, TROPOMI provided critical data to enhance the representation of FNR, HCHO, NO_2 ,
748 $j\text{NO}_2$, and $j\text{O}^1\text{D}$. We utilized TROPOMI's viewing geometry, UV surface albedo, and total ozone overhead
749 from a model to predict $j\text{NO}_2$ and $j\text{O}^1\text{D}$ using look-up tables derived from NCAR's TUV model. To convert
750 TROPOMI tropospheric NO_2 and HCHO columns to their PBL mixing ratios, we employed the
751 MERRA2GMI global transport model, extensively used in various studies. However, the coarse resolution
752 of this model might have introduced underrepresentation issues, which could be mitigated by using higher
753 spatial resolution models in future research.

754 To address the biases associated with TROPOMI observations, we updated comparisons from
755 Verhoelst et al. (2021) and Vigouroux et al. (2020) with a larger dataset of paired TROPOMI and
756 FTIR/MAX-DOAS measurements. TROPOMI retrievals significantly underestimated HCHO and NO_2
757 magnitudes in polluted regions (slope $\sim 0.6 - 0.7$) and moderately overestimated them in pristine areas.
758 These biases were corrected using regression lines, enabling a relatively unbiased application of the data.

759 To build confidence in our product, we propagated TROPOMI HCHO and NO_2 errors to PO_3
760 estimates using a Monte Carlo approach. Results indicated that PO_3 estimates were uncertain ($>50\%$) in
761 clean regions due to a low trace gas signal in TROPOMI retrievals. However, in polluted regions, the errors
762 were more moderate (10-20%) due to the stronger signal.

763 Over the years, extensive efforts have been devoted to measuring various critical atmospheric
764 compounds globally, developing robust atmospheric models, and enhancing satellite retrievals along with
765 their benchmarks. These advancements have enabled us to estimate PO_3 maps within the PBL. Nonetheless,
766 it is crucial to acknowledge some limitations of our work, many of which are the focus of ongoing research
767 within our team:

768 i) The direct measurement of PO₃ using specialized instruments (Cazorla and Brune, 2010;
769 Sadanaga et al., 2017; Sklaveniti et al., 2018) is lacking in most atmospheric composition datasets, limiting
770 our ability to fully understand the effects of assumptions (such as the exclusion of heterogeneous chemistry)
771 made in the box model on PO₃.

772 ii) There is potential for improvement in the parameterization process by employing more
773 sophisticated algorithms, such as neural networks, which could increase the variance explained in the
774 predicted PO₃.

775 iii) The conversion of satellite column data to PBL mixing ratios requires error characterization
776 and the use of finer-resolution models that are comparable in size to the PO₃ grid boxes.

777 iv) Partially cloudy pixels and aerosols can affect photolysis rates, which should be considered in
778 future parameterization efforts.

779 It is important to recognize that PO₃ maps are just one piece of the puzzle when it comes to
780 determining ozone concentrations. Several studies have indicated that accurately representing surface ozone
781 is challenging due to difficulties in representing background ozone, transport, and dry deposition rates.
782 Therefore, we advise against directly linking high PO₃ rates from our product to increased unhealthy ozone
783 exposure. However, our product does provide indications as to whether heightened ozone concentrations
784 are associated with chemistry contributions as opposed to other processes (e.g., meteorology or dry
785 deposition rates). Further investigation using additional tools/data is necessary to gather a full picture of
786 these processes.

787 Despite these limitations, our novel product offers an asset to the atmospheric science community.
788 It provides a more comprehensive understanding of the complexities associated with spatiotemporal
789 variability associated with the non-linear ozone chemistry at a large domain and enhances confidence in
790 high-resolution maps of chemically-produced ozone hotspots.

791 **Financial Support**

792 This study is funded by NASA's ACOMAP/Aura project (grant no. 80NSSC23K1250). The measurements
793 at Paramaribo have been supported by the BMBF (German Ministry of Education and Research) in project
794 ROMIC-II's subproject TroStra (01LG1904A). The NDACC FTIR stations Bremen, Garmisch, Izaña, Ny-
795 Ålesund, Paramaribo, and Karlsruhe have been supported by the German Bundesministerium für Wirtschaft
796 und Energie (BMWi) via DLR5 under grants 50EE1711A, B, and D. The measurements and data analysis
797 at Bremen are supported by the Senate of Bremen. The NCAR FTS observation programs at Thule, GR,
798 Boulder, CO, and Mauna Loa, HI, are supported under contract by the National Aeronautics and Space
799 Administration (NASA). The National Center for Atmospheric Research is sponsored by the National
800 Science Foundation. The Thule effort is also supported by the NSF Office of Polar Programs (OPP).
801 Operations at the Rikubetsu and Tsukuba FTIR sites are supported in part by the GOSAT series project. The
802 Paris TCCON site has received funding from Sorbonne Université, the French research center CNRS, and
803 the French space agency CNES. The Jungfraujoch FTIR data are primarily available thanks to the support
804 provided by the F.R.S. FNRS (Brussels), the GAW-CH program of MeteoSwiss (Zürich), and the HFSJG.ch
805 Foundation (Bern). IUP-Bremen ground-based measurements are funded by DLR-Bonn and received
806 through project 50EE1709A. KNMI ground-based measurements in De Bilt and Cabauw are partly
807 supported by the Ruisdael Observatory project, Dutch Research Council (NWO) contract 184.034.015, by
808 the Netherlands Space Office (NSO) for Sentinel-5p/TROPOMI validation, and by ESA via the EU CAMS
809 project.

810 **Data Availability**

811 TROPOMI satellite data are derived from copernicus Sentinel-5P (processed by ESA), 2021, TROPOMI
812 Level 2 Nitrogen Dioxide total column products. Version 02. European Space Agency.
813 <https://doi.org/10.5270/S5P-9bnp8q8>, and copernicus Sentinel-5P (processed by ESA), 2020, TROPOMI
814 Level 2 Formaldehyde Total Column products. Version 02. European Space Agency.
815 <https://doi.org/10.5270/S5P-vg1i7t0>. The FTIR and MAX-DOAS observations were partly obtained from
816 the Network for the Detection of Atmospheric Composition Change (NDACC) and are available through
817 the NDACC website at <http://www.ndacc.org>. The box model can be obtained from
818 <https://github.com/AirChem/F0AM> (last access: 10 Nov, 2024). The TROPOMI UV DLER can be obtained
819 from https://www.temis.nl/surface/albedo/tropomi_ler.php (last access: 10 Nov 2024).

820 **Competing interests**

821 Bryan N. Duncan is a member of the editorial board of Atmospheric Chemistry and Physics

822 **Acknowledgements**

823 We thank all principal investigators, pilots, and managers who collected the aircraft data used in our
824 research and made them publicly available. We thank the FTIR HCHO measurement team of Thomas
825 Blumenstock, Martine De Mazière, Michel Grutter, James W. Hannigan, Nicholas Jones, Rigel Kivi, Erik
826 Lutsch, Emmanuel Mahieu, Maria Makarova, Isamu Morino, Isao Murata, Tomoo Nagahama, Justus
827 Notholt, Ivan Ortega, Mathias Palm, Amelie Röhlting, Matthias Schneider, Dan Smale, Wolfgang Stremme,
828 Kim String, Youwen Sun, Ralf Sussmann, Yao Té, and Pucai Wang. We thank the Meteorological Service
829 Suriname and Cornelis Becker for their support. The MAX-DOAS data used in this publication were
830 obtained from Alkis Bais, John Burrows, Ka Lok Chan, Michel Grutter, Cheng Liu, Hitoshi Irie, Vinod
831 Kumar, Yugo Kanaya, Ankie Pitters, Claudia Rivera-Cárdenas, Andreas Richter, Michel Van Roozendael,
832 Robert Ryan, Vinayak Sinha, and Thomas Wagner. Fast delivery of MAX-DOAS data tailored to the S5P
833 validation was organized through S5PVT AO project NID-FORVAL. We thank the IISER Mohali
834 atmospheric chemistry facility for supporting the MAX-DOAS measurements at Mohali, India. We thank
835 Julie M. Nicely for providing merged ATOMs observations.

836 **Authors' contributions**

837 AHS designed and implemented the research idea, analyzed the data, made all figures, and wrote the
838 manuscript. TV, CV, GP, SC, and BL provided the paired TROPOMI and benchmark data. Other authors
839 helped with the analysis, the model setup, and interpretation.

840 **References:**

- 841 Ahamad, F., Griffiths, P. T., Latif, M. T., Juneng, L., and Xiang, C. J.: Ozone Trends from Two Decades of
842 Ground Level Observation in Malaysia, *Atmosphere*, 11, 755,
843 <https://doi.org/10.3390/atmos11070755>, 2020.
- 844 Anderson, D. C., Follette-Cook, M. B., Strode, S. A., Nicely, J. M., Liu, J., Ivatt, P. D., and Duncan, B.
845 N.: A machine learning methodology for the generation of a parameterization of the hydroxyl radical,
846 *Geosci. Model Dev.*, 15, 6341–6358, <https://doi.org/10.5194/gmd-15-6341-2022>, 2022.
- 847 Archibald, A. T., Jenkin, M. E., and Shallcross, D. E.: An isoprene mechanism intercomparison, *Atmos.*
848 *Environ.*, 44, 5356–5364, <https://doi.org/10.1016/j.atmosenv.2009.09.016>, 2010.
- 849 Baylon, P., Jaffe, D. A., Hall, S. R., Ullmann, K., Alvarado, M. J., and Lefer, B. L.: Impact of Biomass
850 Burning Plumes on Photolysis Rates and Ozone Formation at the Mount Bachelor Observatory, *J.*
851 *Geophys. Res. Atmos.*, 123, 2272–2284, <https://doi.org/10.1002/2017JD027341>, 2018.

- 852 Beddows, D. C. S., Dall'Osto, M., and Harrison, R. M.: Cluster Analysis of Rural, Urban, and Curbside
853 Atmospheric Particle Size Data, *Environ. Sci. Technol.*, 43, 4694–4700,
854 <https://doi.org/10.1021/es803121t>, 2009.
- 855 Belhout, D., Kerbachi, R., Relvas, H., and Miranda, A. I.: Air quality assessment in Algiers city, *Air*
856 *Qual. Atmos. Health.*, 11, 897–906, <https://doi.org/10.1007/s11869-018-0589-x>, 2018.
- 857 Boraïy, M., El-Metwally, M., Wheida, A., El-Nazer, M., Hassan, S. K., El-Sanabary, F. F., Alfaro, S. C.,
858 Abdelwahab, M., and Borbon, A.: Statistical analysis of the variability of reactive trace gases (SO₂,
859 NO₂ and ozone) in Greater Cairo during dust storm events, *J. Atmos. Chem.*, 80, 227–250,
860 <https://doi.org/10.1007/s10874-023-09449-4>, 2023.
- 861 Bottorff, B., Lew, M. M., Woo, Y., Rickly, P., Rollings, M. D., Deming, B., Anderson, D. C., Wood, E.,
862 Alwe, H. D., Millet, D. B., Weinheimer, A., Tyndall, G., Ortega, J., Dusanter, S., Leonardis, T., Flynn,
863 J., Erickson, M., Alvarez, S., Rivera-Rios, J. C., Shutter, J. D., Keutsch, F., Helmig, D., Wang, W.,
864 Allen, H. M., Slade, J. H., Shepson, P. B., Bertman, S., and Stevens, P. S.: OH, HO₂, and RO₂ radical
865 chemistry in a rural forest environment: measurements, model comparisons, and evidence of a
866 missing radical sink, *Atmos. Chem. Phys.*, 23, 10287–10311, [https://doi.org/10.5194/acp-23-10287-](https://doi.org/10.5194/acp-23-10287-2023)
867 [2023](https://doi.org/10.5194/acp-23-10287-2023), 2023.
- 868 Brune, W. H., Miller, D. O., Thames, A. B., Allen, H. M., Apel, E. C., Blake, D. R., Bui, T. P., Commane,
869 R., Crounse, J. D., Daube, B. C., Diskin, G. S., DiGangi, J. P., Elkins, J. W., Hall, S. R., Hanisco, T.
870 F., Hannun, R. A., Hintsä, E. J., Hornbrook, R. S., Kim, M. J., McKain, K., Moore, F. L., Neuman, J.
871 A., Nicely, J. M., Peischl, J., Ryerson, T. B., St. Clair, J. M., Sweeney, C., Teng, A. P., Thompson, C.,
872 Ullmann, K., Veres, P. R., Wennberg, P. O., and Wolfe, G. M.: Exploring Oxidation in the Remote
873 Free Troposphere: Insights From Atmospheric Tomography (ATom), *J. Geophys. Res. Atmos.*, 125,
874 [e2019JD031685](https://doi.org/10.1029/2019JD031685), <https://doi.org/10.1029/2019JD031685>, 2020.
- 875 Brune, W. H., Miller, D. O., Thames, A. B., Brosius, A. L., Barletta, B., Blake, D. R., Blake, N. J., Chen,
876 G., Choi, Y., Crawford, J. H., Digangi, J. P., Diskin, G., Fried, A., Hall, S. R., Hanisco, T. F., Huey, G.
877 L., Hughes, S. C., Kim, M., Meinardi, S., Montzka, D. D., Pusede, S. E., Schroeder, J. R., Teng, A.,
878 Tanner, D. J., Ullmann, K., Walega, J., Weinheimer, A., Wisthaler, A., and Wennberg, P. O.:
879 Observations of atmospheric oxidation and ozone production in South Korea, *Atmos. Environ.*, 269,
880 [118854](https://doi.org/10.1016/j.atmosenv.2021.118854), <https://doi.org/10.1016/j.atmosenv.2021.118854>, 2022.
- 881 Cazorla, M. and Brune, W. H.: Measurement of Ozone Production Sensor, *Atmos. Meas. Tech.*, 3, 545–
882 [555](https://doi.org/10.5194/amt-3-545-2010), <https://doi.org/10.5194/amt-3-545-2010>, 2010.
- 883 Cazorla, M., Brune, W. H., Ren, X., and Lefer, B.: Direct measurement of ozone production rates in
884 Houston in 2009 and comparison with two estimation methods, *Atmos. Chem. Phys.*, 12, 1203–1212,
885 <https://doi.org/10.5194/acp-12-1203-2012>, 2012.
- 886 Chaichan, M. T., Kazem, H. A., and Abed, T. A.: Traffic and outdoor air pollution levels near highways in
887 Baghdad, Iraq, *Environ. Dev. Sustain.*, 20, 589–603, <https://doi.org/10.1007/s10668-016-9900-x>,
888 2018.
- 889 Chatfield, R. B., Ren, X., Brune, W., and Schwab, J.: Controls on urban ozone production rate as
890 indicated by formaldehyde oxidation rate and nitric oxide, *Atmos. Environ.*, 44, 5395–5406,
891 <https://doi.org/10.1016/j.atmosenv.2010.08.056>, 2010.
- 892 Choi, J., Henze, D. K., Cao, H., Nowlan, C. R., González Abad, G., Kwon, H.-A., Lee, H.-M., Oak, Y. J.,
893 Park, R. J., Bates, K. H., Maasackers, J. D., Wisthaler, A., and Weinheimer, A. J.: An Inversion
894 Framework for Optimizing Non-Methane VOC Emissions Using Remote Sensing and Airborne

- 895 Observations in Northeast Asia During the KORUS-AQ Field Campaign, *J. Geophys. Res. Atmos.*,
896 127, e2021JD035844, <https://doi.org/10.1029/2021JD035844>, 2022.
- 897 Choi, S., Lamsal, L. N., Follette-Cook, M., Joiner, J., Krotkov, N. A., Swartz, W. H., Pickering, K. E.,
898 Loughner, C. P., Appel, W., Pfister, G., Saide, P. E., Cohen, R. C., Weinheimer, A. J., and Herman, J.
899 R.: Assessment of NO₂ observations during DISCOVER-AQ and KORUS-AQ field campaigns,
900 *Atmos. Meas. Tech.*, 13, 2523–2546, <https://doi.org/10.5194/amt-13-2523-2020>, 2020.
- 901 Choi, Y. and Souri, A. H.: Chemical condition and surface ozone in large cities of Texas during the last
902 decade: Observational evidence from OMI, CAMS, and model analysis, *Remote Sens. Environ.*, 168,
903 90–101, <https://doi.org/10.1016/j.rse.2015.06.026>, 2015a.
- 904 Choi, Y. and Souri, A. H.: Seasonal behavior and long-term trends of tropospheric ozone, its precursors
905 and chemical conditions over Iran: A view from space, *Atmos. Environ.*, 106, 232–240,
906 <https://doi.org/10.1016/j.atmosenv.2015.02.012>, 2015b.
- 907 Choi, Y., Kim, H., Tong, D., and Lee, P.: Summertime weekly cycles of observed and modeled NO_x and
908 O₃ concentrations as a function of satellite-derived ozone production sensitivity and land use types
909 over the Continental United States, *Atmos. Chem. Phys.*, 12, 6291–6307, <https://doi.org/10.5194/acp-12-6291-2012>, 2012.
- 911 Colombi, N. K., Jacob, D. J., Yang, L. H., Zhai, S., Shah, V., Grange, S. K., Yantosca, R. M., Kim, S., and
912 Liao, H.: Why is ozone in South Korea and the Seoul metropolitan area so high and increasing?,
913 *Atmos. Chem. Phys.*, 23, 4031–4044, <https://doi.org/10.5194/acp-23-4031-2023>, 2023.
- 914 Crawford, J. H., Ahn, J.-Y., Al-Saadi, J., Chang, L., Emmons, L. K., Kim, J., Lee, G., Park, J.-H., Park, R.
915 J., Woo, J. H., Song, C.-K., Hong, J.-H., Hong, Y.-D., Lefer, B. L., Lee, M., Lee, T., Kim, S., Min, K.-
916 E., Yum, S. S., Shin, H. J., Kim, Y.-W., Choi, J.-S., Park, J.-S., Szykman, J. J., Long, R. W., Jordan, C.
917 E., Simpson, I. J., Fried, A., Dibb, J. E., Cho, S., and Kim, Y. P.: The Korea–United States Air Quality
918 (KORUS-AQ) field study, *Elem. Sci. Anth.*, 9, 00163, <https://doi.org/10.1525/elementa.2020.00163>,
919 2021.
- 920 De Smedt, I., Pinardi, G., Vigouroux, C., Compernelle, S., Bais, A., Benavent, N., Boersma, F., Chan, K.-
921 L., Donner, S., Eichmann, K.-U., Hedelt, P., Hendrick, F., Irie, H., Kumar, V., Lambert, J.-C.,
922 Langerock, B., Lerot, C., Liu, C., Loyola, D., Piters, A., Richter, A., Rivera Cárdenas, C., Romahn, F.,
923 Ryan, R. G., Sinha, V., Theys, N., Vlietinck, J., Wagner, T., Wang, T., Yu, H., and Van Roozendaal,
924 M.: Comparative assessment of TROPOMI and OMI formaldehyde observations and validation
925 against MAX-DOAS network column measurements, *Atmos. Chem. Phys.*, 21, 12561–12593,
926 <https://doi.org/10.5194/acp-21-12561-2021>, 2021.
- 927 DiMaria, C. A., Jones, D. B. A., Worden, H., Bloom, A. A., Bowman, K., Stavrou, T., Miyazaki, K.,
928 Worden, J., Guenther, A., Sarkar, C., Seco, R., Park, J.-H., Tota, J., Alves, E. G., and Ferracci, V.:
929 Optimizing the Isoprene Emission Model MEGAN With Satellite and Ground-Based Observational
930 Constraints, *J. Geophys. Res. Atmos.*, 128, e2022JD037822, <https://doi.org/10.1029/2022JD037822>,
931 2023.
- 932 Duncan, B. N. and Chameides, W. L.: Effects of urban emission control strategies on the export of ozone
933 and ozone precursors from the urban atmosphere to the troposphere, *J. Geophys. Res. Atmos.*, 103,
934 28159–28179, <https://doi.org/10.1029/98JD02145>, 1998.
- 935 Duncan, B. N., Strahan, S. E., Yoshida, Y., Steenrod, S. D., and Livesey, N.: Model study of the cross-
936 tropopause transport of biomass burning pollution, *Atmos. Chem. Phys.*, 7, 3713–3736,
937 <https://doi.org/10.5194/acp-7-3713-2007>, 2007.

- 938 Duncan, B. N., Yoshida, Y., Olson, J. R., Sillman, S., Martin, R. V., Lamsal, L., Hu, Y., Pickering, K. E.,
 939 Retscher, C., Allen, D. J., and Crawford, J. H.: Application of OMI observations to a space-based
 940 indicator of NO_x and VOC controls on surface ozone formation, *Atmos. Environ.*, 44, 2213–2223,
 941 <https://doi.org/10.1016/j.atmosenv.2010.03.010>, 2010.
- 942 Fleming, Z. L., Doherty, R. M., von Schneidemesser, E., Malley, C. S., Cooper, O. R., Pinto, J. P., Colette,
 943 A., Xu, X., Simpson, D., Schultz, M. G., Lefohn, A. S., Hamad, S., Moolla, R., Solberg, S., and Feng,
 944 Z.: Tropospheric Ozone Assessment Report: Present-day ozone distribution and trends relevant to
 945 human health, *Elem. Sci. Anth.*, 6, 12, <https://doi.org/10.1525/elementa.273>, 2018.
- 946 Gaudel, A., Cooper, O. R., Ancellet, G., Barret, B., Boynard, A., Burrows, J. P., Clerbaux, C., Coheur, P.-
 947 F., Cuesta, J., Cuevas, E., Doniki, S., Dufour, G., Ebojje, F., Foret, G., Garcia, O., Granados-Muñoz,
 948 M. J., Hannigan, J. W., Hase, F., Hassler, B., Huang, G., Hurtmans, D., Jaffe, D., Jones, N.,
 949 Kalabokas, P., Kerridge, B., Kulawik, S., Latter, B., Leblanc, T., Le Flochmoën, E., Lin, W., Liu, J.,
 950 Liu, X., Mahieu, E., McClure-Begley, A., Neu, J. L., Osman, M., Palm, M., Petetin, H.,
 951 Petropavlovskikh, I., Querel, R., Rahpoe, N., Rozanov, A., Schultz, M. G., Schwab, J., Siddans, R.,
 952 Smale, D., Steinbacher, M., Tanimoto, H., Tarasick, D. W., Thouret, V., Thompson, A. M., Trickl, T.,
 953 Weatherhead, E., Wespes, C., Worden, H. M., Vigouroux, C., Xu, X., Zeng, G., and Ziemke, J.:
 954 Tropospheric Ozone Assessment Report: Present-day distribution and trends of tropospheric ozone
 955 relevant to climate and global atmospheric chemistry model evaluation, *Elem. Sci. Anth.*, 6, 39,
 956 <https://doi.org/10.1525/elementa.291>, 2018.
- 957 Gerasopoulos, E., Kouvarakis, G., Vrekoussis, M., Donoussis, C., Mihalopoulos, N., and Kanakidou, M.:
 958 Photochemical ozone production in the Eastern Mediterranean, *Atmos. Environ.*, 40, 3057–3069,
 959 <https://doi.org/10.1016/j.atmosenv.2005.12.061>, 2006.
- 960 Govender, P. and Sivakumar, V.: Application of k-means and hierarchical clustering techniques for
 961 analysis of air pollution: A review (1980–2019), *Atmos. Pollut. Res.*, 11, 40–56,
 962 <https://doi.org/10.1016/j.apr.2019.09.009>, 2020.
- 963 Jeon, W., Choi, Y., Souri, A. H., Roy, A., Diao, L., Pan, S., Lee, H. W., and Lee, S.-H.: Identification of
 964 chemical fingerprints in long-range transport of burning induced upper tropospheric ozone from
 965 Colorado to the North Atlantic Ocean, *Sci. Total Environ.*, 613–614, 820–828,
 966 <https://doi.org/10.1016/j.scitotenv.2017.09.177>, 2018.
- 967 Jin, X., Fiore, A. M., Murray, L. T., Valin, L. C., Lamsal, L. N., Duncan, B., Folkert Boersma, K., De
 968 Smedt, I., Abad, G. G., Chance, K., and Tonnesen, G. S.: Evaluating a Space-Based Indicator of
 969 Surface Ozone-NO_x-VOC Sensitivity Over Midlatitude Source Regions and Application to Decadal
 970 Trends, *J. Geophys. Res. Atmos.*, 122, 10,439-10,461, <https://doi.org/10.1002/2017JD026720>, 2017.
- 971 Johnson, M. S., Souri, A. H., Philip, S., Kumar, R., Naeger, A., Geddes, J., Judd, L., Janz, S., Chong, H.,
 972 and Sullivan, J.: Satellite remote-sensing capability to assess tropospheric-column ratios of
 973 formaldehyde and nitrogen dioxide: case study during the Long Island Sound Tropospheric Ozone
 974 Study 2018 (LISTOS 2018) field campaign, *Atmos. Meas. Tech.*, 16, 2431–2454,
 975 <https://doi.org/10.5194/amt-16-2431-2023>, 2023.
- 976 Kim, S.-W., McDonald, B. C., Seo, S., Kim, K.-M., and Trainer, M.: Understanding the Paths of Surface
 977 Ozone Abatement in the Los Angeles Basin, *J. Geophys. Res. Atmos.*, 127, e2021JD035606,
 978 <https://doi.org/10.1029/2021JD035606>, 2022.
- 979 Kleinman, L. I., Daum, P. H., Imre, D., Lee, Y.-N., Nunnermacker, L. J., Springston, S. R., Weinstein-
 980 Lloyd, J., and Rudolph, J.: Ozone production rate and hydrocarbon reactivity in 5 urban areas: A
 981 cause of high ozone concentration in Houston, *Geophys. Res. Lett.*, 29, 105-1-105-4,
 982 <https://doi.org/10.1029/2001GL014569>, 2002.

- 983 Kusumaningtyas, S. D. A., Tonokura, K., Muharsyah, R., Gunawan, D., Sopaheluwakan, A., Iriana, W.,
984 Lestari, P., Permadi, D. A., Rahmawati, R., and Samputra, N. A. R.: Comprehensive analysis of long-
985 term trends, meteorological influences, and ozone formation sensitivity in the Jakarta Greater Area,
986 *Sci. Rep.*, 14, 9605, <https://doi.org/10.1038/s41598-024-60374-2>, 2024.
- 987 Lelieveld, J., Hoor, P., Jöckel, P., Pozzer, A., Hadjinicolaou, P., Cammas, J.-P., and Beirle, S.: Severe
988 ozone air pollution in the Persian Gulf region, *Atmos. Chem. Phys.*, 9, 1393–1406,
989 <https://doi.org/10.5194/acp-9-1393-2009>, 2009.
- 990 Li, K., Jacob, D. J., Liao, H., Shen, L., Zhang, Q., and Bates, K. H.: Anthropogenic drivers of 2013–2017
991 trends in summer surface ozone in China, *Proc. Natl. Acad. Sci.*, 116, 422–427,
992 <https://doi.org/10.1073/pnas.1812168116>, 2019.
- 993 Marais, E. A., Jacob, D. J., Guenther, A., Chance, K., Kurosu, T. P., Murphy, J. G., Reeves, C. E., and
994 Pye, H. O. T.: Improved model of isoprene emissions in Africa using Ozone Monitoring Instrument
995 (OMI) satellite observations of formaldehyde: implications for oxidants and particulate matter,
996 *Atmos. Chem. Phys.*, 14, 7693–7703, <https://doi.org/10.5194/acp-14-7693-2014>, 2014.
- 997 Martin, R. V., Fiore, A. M., and Van Donkelaar, A.: Space-based diagnosis of surface ozone sensitivity to
998 anthropogenic emissions, *Geophys. Res. Lett.*, 31, <https://doi.org/10.1029/2004GL019416>, 2004.
- 999 Marvin, M. R., Wolfe, G. M., Salawitch, R. J., Canty, T. P., Roberts, S. J., Travis, K. R., Aikin, K. C., de
1000 Gouw, J. A., Graus, M., Hanisco, T. F., Holloway, J. S., Hübler, G., Kaiser, J., Keutsch, F. N., Peischl,
1001 J., Pollack, I. B., Roberts, J. M., Ryerson, T. B., Veres, P. R., and Warneke, C.: Impact of evolving
1002 isoprene mechanisms on simulated formaldehyde: An inter-comparison supported by in situ
1003 observations from SENEX, *Atmos. Environ.*, 164, 325–336,
1004 <https://doi.org/10.1016/j.atmosenv.2017.05.049>, 2017.
- 1005 Mazzuca, G. M., Ren, X., Loughner, C. P., Estes, M., Crawford, J. H., Pickering, K. E., Weinheimer, A. J.,
1006 and Dickerson, R. R.: Ozone production and its sensitivity to NO_x and VOCs: results from the
1007 DISCOVER-AQ field experiment, Houston 2013, *Atmos. Chem. Phys.*, 16, 14463–14474,
1008 <https://doi.org/10.5194/acp-16-14463-2016>, 2016.
- 1009 Miller, D. O. and Brune, W. H.: Investigating the Understanding of Oxidation Chemistry Using 20 Years
1010 of Airborne OH and HO₂ Observations, *J. Geophys. Res. Atmos.*, 127, e2021JD035368,
1011 <https://doi.org/10.1029/2021JD035368>, 2022.
- 1012 Mills, G., Pleijel, H., Malley, C. S., Sinha, B., Cooper, O. R., Schultz, M. G., Neufeld, H. S., Simpson, D.,
1013 Sharps, K., Feng, Z., Gerosa, G., Harmens, H., Kobayashi, K., Saxena, P., Paoletti, E., Sinha, V., and
1014 Xu, X.: Tropospheric Ozone Assessment Report: Present-day tropospheric ozone distribution and
1015 trends relevant to vegetation, *Elem. Sci. Anth.*, 6, 47, <https://doi.org/10.1525/elementa.302>, 2018.
- 1016 Miyazaki, K., Eskes, H., Sudo, K., Boersma, K. F., Bowman, K., and Kanaya, Y.: Decadal changes in
1017 global surface NO_x emissions from multi-constituent satellite data assimilation, *Atmos. Chem. Phys.*,
1018 17, 807–837, <https://doi.org/10.5194/acp-17-807-2017>, 2017.
- 1019 Orbe, C., Oman, L. D., Strahan, S. E., Waugh, D. W., Pawson, S., Takacs, L. L., and Molod, A. M.: Large-
1020 Scale Atmospheric Transport in GEOS Replay Simulations, *J. Adv. Model. Earth Syst.*, 9, 2545–2560,
1021 <https://doi.org/10.1002/2017MS001053>, 2017.
- 1022 Pan, S., Roy, A., Choi, Y., Eslami, E., Thomas, S., Jiang, X., and Gao, H. O.: Potential impacts of electric
1023 vehicles on air quality and health endpoints in the Greater Houston Area in 2040, *Atmos. Environ.*,
1024 207, 38–51, <https://doi.org/10.1016/j.atmosenv.2019.03.022>, 2019.

- 1025 Ren, X., van Duin, D., Cazorla, M., Chen, S., Mao, J., Zhang, L., Brune, W. H., Flynn, J. H., Grossberg,
1026 N., Lefer, B. L., Rappenglück, B., Wong, K. W., Tsai, C., Stutz, J., Dibb, J. E., Thomas Jobson, B.,
1027 Luke, W. T., and Kelley, P.: Atmospheric oxidation chemistry and ozone production: Results from
1028 SHARP 2009 in Houston, Texas, *J. Geophys. Res. Atmos.*, 118, 5770–5780,
1029 <https://doi.org/10.1002/jgrd.50342>, 2013.
- 1030 Roberts, G., Wooster, M. J., and Lagoudakis, E.: Annual and diurnal african biomass burning temporal
1031 dynamics, *Biogeosciences*, 6, 849–866, <https://doi.org/10.5194/bg-6-849-2009>, 2009.
- 1032 Sadanaga, Y., Kawasaki, S., Tanaka, Y., Kajii, Y., and Bandow, H.: New System for Measuring the
1033 Photochemical Ozone Production Rate in the Atmosphere, *Environ. Sci. Technol.*, 51, 2871–2878,
1034 <https://doi.org/10.1021/acs.est.6b04639>, 2017.
- 1035 Sakamoto, Y., Shoji, K., Bui, M. T., Phạm, T. H., Vu, T. A., Ly, B. T., and Kajii, Y.: Air quality study in
1036 Hanoi, Vietnam in 2015–2016 based on a one-year observation of NO_x, O₃, CO and a one-week
1037 observation of VOCs, *Atmos. Pollut. Res.*, 9, 544–551, <https://doi.org/10.1016/j.apr.2017.12.001>,
1038 2018.
- 1039 Schroeder, J. R., Crawford, J. H., Ahn, J.-Y., Chang, L., Fried, A., Walega, J., Weinheimer, A., Montzka,
1040 D. D., Hall, S. R., Ullmann, K., Wisthaler, A., Mikoviny, T., Chen, G., Blake, D. R., Blake, N. J.,
1041 Hughes, S. C., Meinardi, S., Diskin, G., Digangi, J. P., Choi, Y., Pusede, S. E., Huey, G. L., Tanner, D.
1042 J., Kim, M., and Wennberg, P.: Observation-based modeling of ozone chemistry in the Seoul
1043 metropolitan area during the Korea-United States Air Quality Study (KORUS-AQ), *Elem. Sci. Anth.*,
1044 8, 3, <https://doi.org/10.1525/elementa.400>, 2020.
- 1045 Schroeder, J. R., Crawford, J. H., Fried, A., Walega, J., Weinheimer, A., Wisthaler, A., Müller, M.,
1046 Mikoviny, T., Chen, G., Shook, M., Blake, D. R., and Tonnesen, G. S.: New insights into the column
1047 CH₂O/NO₂ ratio as an indicator of near-surface ozone sensitivity, *J. Geophys. Res. Atmos.*, 122,
1048 8885–8907, <https://doi.org/10.1002/2017JD026781>, 2017.
- 1049 Sillman, S. and He, D.: Some theoretical results concerning O₃-NO_x-VOC chemistry and NO_x-VOC
1050 indicators, *J. Geophys. Res. Atmos.*, 107, ACH 26-1-ACH 26-15,
1051 <https://doi.org/10.1029/2001JD001123>, 2002.
- 1052 Silva, S. J., Heald, C. L., Ravela, S., Mammarella, I., and Munger, J. W.: A Deep Learning
1053 Parameterization for Ozone Dry Deposition Velocities, *Geophys. Res. Lett.*, 46, 983–989,
1054 <https://doi.org/10.1029/2018GL081049>, 2019.
- 1055 Simpson, W. R., Brown, S. S., Saiz-Lopez, A., Thornton, J. A., and von Glasow, R.: Tropospheric
1056 Halogen Chemistry: Sources, Cycling, and Impacts, *Chem. Rev.*, 115, 4035–4062,
1057 <https://doi.org/10.1021/cr5006638>, 2015.
- 1058 Singh, H. B., Brune, W. H., Crawford, J. H., Flocke, F., and Jacob, D. J.: Chemistry and transport of
1059 pollution over the Gulf of Mexico and the Pacific: spring 2006 INTEX-B campaign overview and
1060 first results, *Atmos. Chem. Phys.*, 9, 2301–2318, <https://doi.org/10.5194/acp-9-2301-2009>, 2009.
- 1061 Sklaveniti, S., Locoge, N., Stevens, P. S., Wood, E., Kundu, S., and Dusanter, S.: Development of an
1062 instrument for direct ozone production rate measurements: measurement reliability and current
1063 limitations, *Atmos. Meas. Tech.*, 11, 741–761, <https://doi.org/10.5194/amt-11-741-2018>, 2018.
- 1064 Souri, A. H., Chance, K., Bak, J., Nowlan, C. R., González Abad, G., Jung, Y., Wong, D. C., Mao, J., and
1065 Liu, X.: Unraveling pathways of elevated ozone induced by the 2020 lockdown in Europe by an
1066 observationally constrained regional model using TROPOMI, *Atmos. Chem. Phys.*, 21, 18227–18245,
1067 <https://doi.org/10.5194/acp-21-18227-2021>, 2021.

- 1068 Souri, A. H., Choi, Y., Jeon, W., Li, X., Pan, S., Diao, L., and Westenbarger, D. A.: Constraining NO_x
1069 emissions using satellite NO₂ measurements during 2013 DISCOVER-AQ Texas campaign, *Atmos.*
1070 *Environ.*, 131, 371–381, <https://doi.org/10.1016/j.atmosenv.2016.02.020>, 2016a.
- 1071 Souri, A. H., Choi, Y., Li, X., Kotsakis, A., and Jiang, X.: A 15-year climatology of wind pattern impacts
1072 on surface ozone in Houston, Texas, *Atmos. Res.*, 174–175, 124–134,
1073 <https://doi.org/10.1016/j.atmosres.2016.02.007>, 2016b.
- 1074 Souri, A. H., Duncan, B. N., Strode, S. A., Anderson, D. C., Manyin, M. E., Liu, J., Oman, L. D., Zhang,
1075 Z., and Weir, B.: Enhancing Long-Term Trend Simulation of Global Tropospheric OH and Its Drivers
1076 from 2005-2019: A Synergistic Integration of Model Simulations and Satellite Observations,
1077 *EGU*sphere, 1–37, <https://doi.org/10.5194/egusphere-2024-410>, 2024.
- 1078 Souri, A. H., Johnson, M. S., Wolfe, G. M., Crawford, J. H., Fried, A., Wisthaler, A., Brune, W. H., Blake,
1079 D. R., Weinheimer, A. J., Verhoelst, T., Compernelle, S., Pinardi, G., Vigouroux, C., Langerock, B.,
1080 Choi, S., Lamsal, L., Zhu, L., Sun, S., Cohen, R. C., Min, K.-E., Cho, C., Philip, S., Liu, X., and
1081 Chance, K.: Characterization of errors in satellite-based HCHO/NO₂ tropospheric column ratios with
1082 respect to chemistry, column-to-PBL translation, spatial representation, and retrieval uncertainties,
1083 *Atmos. Chem. Phys.*, 23, 1963–1986, <https://doi.org/10.5194/acp-23-1963-2023>, 2023.
- 1084 Souri, A. H., Nowlan, C. R., González Abad, G., Zhu, L., Blake, D. R., Fried, A., Weinheimer, A. J.,
1085 Wisthaler, A., Woo, J.-H., Zhang, Q., Chan Miller, C. E., Liu, X., and Chance, K.: An inversion of
1086 NO_x and non-methane volatile organic compound (NMVOC) emissions using satellite observations
1087 during the KORUS-AQ campaign and implications for surface ozone over East Asia, *Atmos. Chem.*
1088 *Phys.*, 20, 9837–9854, <https://doi.org/10.5194/acp-20-9837-2020>, 2020b.
- 1089 Souri, A. H., Nowlan, C. R., Wolfe, G. M., Lamsal, L. N., Chan Miller, C. E., Abad, G. G., Janz, S. J.,
1090 Fried, A., Blake, D. R., Weinheimer, A. J., Diskin, G. S., Liu, X., and Chance, K.: Revisiting the
1091 effectiveness of HCHO/NO₂ ratios for inferring ozone sensitivity to its precursors using high
1092 resolution airborne remote sensing observations in a high ozone episode during the KORUS-AQ
1093 campaign, *Atmos. Environ.*, 224, 117341, <https://doi.org/10.1016/j.atmosenv.2020.117341>, 2020a.
- 1094 Stanier, C. O., Pierce, R. B., Abdi-Oskouei, M., Adelman, Z. E., Al-Saadi, J., Alwe, H. D., Bertram, T. H.,
1095 Carmichael, G. R., Christiansen, M. B., Cleary, P. A., Czarnetzki, A. C., Dickens, A. F., Fuoco, M. A.,
1096 Hughes, D. D., Hupy, J. P., Janz, S. J., Judd, L. M., Kenski, D., Kowalewski, M. G., Long, R. W.,
1097 Millet, D. B., Novak, G., Roozitalab, B., Shaw, S. L., Stone, E. A., Szykman, J., Valin, L., Vermeuel,
1098 M., Wagner, T. J., Whitehill, A. R., and Williams, D. J.: Overview of the Lake Michigan Ozone Study
1099 2017, *Bull. Am. Meteorol. Soc.*, 102, E2207–E2225, <https://doi.org/10.1175/BAMS-D-20-0061.1>,
1100 2021.
- 1101 Stavrakou, T., Müller, J.-F., Bauwens, M., De Smedt, I., Lerot, C., Van Roozendaal, M., Coheur, P.-F.,
1102 Clerbaux, C., Boersma, K. F., van der A, R., and Song, Y.: Substantial Underestimation of Post-
1103 Harvest Burning Emissions in the North China Plain Revealed by Multi-Species Space Observations,
1104 *Sci. Rep.*, 6, 32307, <https://doi.org/10.1038/srep32307>, 2016.
- 1105 Strode, S. A., Ziemke, J. R., Oman, L. D., Lamsal, L. N., Olsen, M. A., and Liu, J.: Global changes in the
1106 diurnal cycle of surface ozone, *Atmos. Environ.*, 199, 323–333,
1107 <https://doi.org/10.1016/j.atmosenv.2018.11.028>, 2019.
- 1108 Tao, M., Fiore, A. M., Jin, X., Schiferl, L. D., Commane, R., Judd, L. M., Janz, S., Sullivan, J. T., Miller,
1109 P. J., Karambelas, A., Davis, S., Tzortziou, M., Valin, L., Whitehill, A., Civerolo, K., and Tian, Y.:
1110 Investigating Changes in Ozone Formation Chemistry during Summertime Pollution Events over the
1111 Northeastern United States, *Environ. Sci. Technol.*, 56, 15312–15327,
1112 <https://doi.org/10.1021/acs.est.2c02972>, 2022.

- 1113 Thompson, A. M., Balashov, N. V., Witte, J. C., Coetzee, J. G. R., Thouret, V., and Posny, F.:
 1114 Tropospheric ozone increases over the southern Africa region: bellwether for rapid growth in
 1115 Southern Hemisphere pollution?, *Atmos. Chem. Phys.*, 14, 9855–9869, [https://doi.org/10.5194/acp-](https://doi.org/10.5194/acp-14-9855-2014)
 1116 14-9855-2014, 2014.
- 1117 Thompson, C. R., Wofsy, S. C., Prather, M. J., Newman, P. A., Hanisco, T. F., Ryerson, T. B., Fahey, D.
 1118 W., Apel, E. C., Brock, C. A., Brune, W. H., Froyd, K., Katich, J. M., Nicely, J. M., Peischl, J., Ray,
 1119 E., Veres, P. R., Wang, S., Allen, H. M., Asher, E., Bian, H., Blake, D., Bourgeois, I., Budney, J., Bui,
 1120 T. P., Butler, A., Campuzano-Jost, P., Chang, C., Chin, M., Commane, R., Correa, G., Crouse, J. D.,
 1121 Daube, B., Dibb, J. E., DiGangi, J. P., Diskin, G. S., Dollner, M., Elkins, J. W., Fiore, A. M., Flynn, C.
 1122 M., Guo, H., Hall, S. R., Hannun, R. A., Hills, A., Hintsa, E. J., Hodzic, A., Hornbrook, R. S., Huey,
 1123 L. G., Jimenez, J. L., Keeling, R. F., Kim, M. J., Kupc, A., Lacey, F., Lait, L. R., Lamarque, J.-F., Liu,
 1124 J., McKain, K., Meinardi, S., Miller, D. O., Montzka, S. A., Moore, F. L., Morgan, E. J., Murphy, D.
 1125 M., Murray, L. T., Nault, B. A., Neuman, J. A., Nguyen, L., González, Y., Rollins, A., Rosenlof, K.,
 1126 Sargent, M., Schill, G., Schwarz, J. P., Clair, J. M. S., Steenrod, S. D., Stephens, B. B., Strahan, S. E.,
 1127 Strode, S. A., Sweeney, C., Thames, A. B., Ullmann, K., Wagner, N., Weber, R., Weinzierl, B.,
 1128 Wennberg, P. O., Williamson, C. J., Wolfe, G. M., and Zeng, L.: The NASA Atmospheric
 1129 Tomography (ATom) Mission: Imaging the Chemistry of the Global Atmosphere, *Bull. Am. Meteorol.*
 1130 *Soc.*, 103, E761–E790, <https://doi.org/10.1175/BAMS-D-20-0315.1>, 2022.
- 1131 Thornton, J. A., Wooldridge, P. J., Cohen, R. C., Martinez, M., Harder, H., Brune, W. H., Williams, E. J.,
 1132 Roberts, J. M., Fehsenfeld, F. C., Hall, S. R., Shetter, R. E., Wert, B. P., and Fried, A.: Ozone
 1133 production rates as a function of NO_x abundances and HO_x production rates in the Nashville urban
 1134 plume, *J. Geophys. Res. Atmos.*, 107, ACH 7-1-ACH 7-17, <https://doi.org/10.1029/2001JD000932>,
 1135 2002.
- 1136 Tibshirani, R.: Regression Shrinkage and Selection via the Lasso, *J. R. Stat. B (Methodological)*, 58, 267–
 1137 288, 1996.
- 1138 Tilstra, L. G., de Graaf, M., Trees, V., Litvinov, P., Dubovik, O., and Stammes, P.: A directional surface
 1139 reflectance climatology determined from TROPOMI observations, *Atmos. Meas. Tech. Discussions*,
 1140 1–29, <https://doi.org/10.5194/amt-2023-222>, 2023.
- 1141 Tonnesen, G. S. and Dennis, R. L.: Analysis of radical propagation efficiency to assess ozone sensitivity
 1142 to hydrocarbons and NO_x : 1. Local indicators of instantaneous odd oxygen production sensitivity, *J.*
 1143 *Geophys. Res.*, 105, 9213–9225, <https://doi.org/10.1029/1999JD900371>, 2000a.
- 1144 Tonnesen, G. S. and Dennis, R. L.: Analysis of radical propagation efficiency to assess ozone sensitivity
 1145 to hydrocarbons and NO_x : 2. Long-lived species as indicators of ozone concentration sensitivity, *J.*
 1146 *Geophys. Res.*, 105, 9227–9241, <https://doi.org/10.1029/1999JD900372>, 2000b.
- 1147 van der Velde, I. R., van der Werf, G. R., Houweling, S., Eskes, H. J., Veefkind, J. P., Borsdorff, T., and
 1148 Aben, I.: Biomass burning combustion efficiency observed from space using measurements of CO
 1149 and NO₂ by the TROPospheric Monitoring Instrument (TROPOMI), *Atmos. Chem. Phys.*, 21, 597–
 1150 616, <https://doi.org/10.5194/acp-21-597-2021>, 2021.
- 1151 van Geffen, J., Eskes, H., Compernelle, S., Pinardi, G., Verhoelst, T., Lambert, J.-C., Sneep, M., ter
 1152 Linden, M., Ludewig, A., Boersma, K. F., and Veefkind, J. P.: Sentinel-5P TROPOMI NO₂ retrieval:
 1153 impact of version v2.2 improvements and comparisons with OMI and ground-based data, *Atmos.*
 1154 *Meas. Tech.*, 15, 2037–2060, <https://doi.org/10.5194/amt-15-2037-2022>, 2022.
- 1155 Veefkind, J. P., Aben, I., McMullan, K., Förster, H., de Vries, J., Otter, G., Claas, J., Eskes, H. J., de Haan,
 1156 J. F., Kleipool, Q., van Weele, M., Hasekamp, O., Hoogeveen, R., Landgraf, J., Snel, R., Tol, P.,
 1157 Ingmann, P., Voors, R., Kruizinga, B., Vink, R., Visser, H., and Levelt, P. F.: TROPOMI on the ESA

- 1158 Sentinel-5 Precursor: A GMES mission for global observations of the atmospheric composition for
 1159 climate, air quality and ozone layer applications, *Remote Sens. Environ.*, 120, 70–83,
 1160 <https://doi.org/10.1016/j.rse.2011.09.027>, 2012.
- 1161 Verhoelst, T., Compernelle, S., Pinardi, G., Lambert, J.-C., Eskes, H. J., Eichmann, K.-U., Fjæraa, A. M.,
 1162 Granville, J., Niemeijer, S., Cede, A., Tiefengraber, M., Hendrick, F., Pazmiño, A., Bais, A.,
 1163 Bazureau, A., Boersma, K. F., Bogner, K., Dehn, A., Donner, S., Elokhov, A., Gebetsberger, M.,
 1164 Goutail, F., Grutter de la Mora, M., Gruzdev, A., Gratsea, M., Hansen, G. H., Irie, H., Jepsen, N.,
 1165 Kanaya, Y., Karagkiozidis, D., Kivi, R., Kreher, K., Levelt, P. F., Liu, C., Müller, M., Navarro Comas,
 1166 M., PETERS, A. J. M., Pommereau, J.-P., Portafaix, T., Prados-Roman, C., Puentedura, O., Querel, R.,
 1167 Remmers, J., Richter, A., Rimmer, J., Rivera Cárdenas, C., Saavedra de Miguel, L., Sinyakov, V. P.,
 1168 Stremme, W., Strong, K., Van Roozendaal, M., Veeffkind, J. P., Wagner, T., Wittrock, F., Yela
 1169 González, M., and Zehner, C.: Ground-based validation of the Copernicus Sentinel-5P TROPOMI
 1170 NO₂ measurements with the NDACC ZSL-DOAS, MAX-DOAS and Pandonia global networks,
 1171 *Atmos. Meas. Tech.*, 14, 481–510, <https://doi.org/10.5194/amt-14-481-2021>, 2021.
- 1172 Vigouroux, C., Langerock, B., Bauer Aquino, C. A., Blumenstock, T., Cheng, Z., De Mazière, M., De
 1173 Smedt, I., Grutter, M., Hannigan, J. W., Jones, N., Kivi, R., Loyola, D., Lutsch, E., Mahieu, E.,
 1174 Makarova, M., Metzger, J.-M., Morino, I., Murata, I., Nagahama, T., Notholt, J., Ortega, I., Palm, M.,
 1175 Pinardi, G., Röhling, A., Smale, D., Stremme, W., Strong, K., Sussmann, R., Tè, Y., van Roozendaal,
 1176 M., Wang, P., and Winkler, H.: TROPOMI–Sentinel-5 Precursor formaldehyde validation using an
 1177 extensive network of ground-based Fourier-transform infrared stations, *Atmos. Meas. Tech.*, 13,
 1178 3751–3767, <https://doi.org/10.5194/amt-13-3751-2020>, 2020.
- 1179 Wang, T., Xue, L., Brimblecombe, P., Lam, Y. F., Li, L., and Zhang, L.: Ozone pollution in China: A
 1180 review of concentrations, meteorological influences, chemical precursors, and effects, *Sci. Total*
 1181 *Environ.*, 575, 1582–1596, <https://doi.org/10.1016/j.scitotenv.2016.10.081>, 2017.
- 1182 Wang, W., Parrish, D. D., Li, X., Shao, M., Liu, Y., Mo, Z., Lu, S., Hu, M., Fang, X., Wu, Y., Zeng, L.,
 1183 and Zhang, Y.: Exploring the drivers of the increased ozone production in Beijing in summertime
 1184 during 2005–2016, *Atmos. Chem. Phys.*, 20, 15617–15633, [https://doi.org/10.5194/acp-20-15617-](https://doi.org/10.5194/acp-20-15617-2020)
 1185 2020, 2020.
- 1186 Warneke, C., Trainer, M., de Gouw, J. A., Parrish, D. D., Fahey, D. W., Ravishankara, A. R., Middlebrook,
 1187 A. M., Brock, C. A., Roberts, J. M., Brown, S. S., Neuman, J. A., Lerner, B. M., Lack, D., Law, D.,
 1188 Hübler, G., Pollack, I., Sjostedt, S., Ryerson, T. B., Gilman, J. B., Liao, J., Holloway, J., Peischl, J.,
 1189 Nowak, J. B., Aikin, K. C., Min, K.-E., Washenfelder, R. A., Graus, M. G., Richardson, M.,
 1190 Markovic, M. Z., Wagner, N. L., Welti, A., Veres, P. R., Edwards, P., Schwarz, J. P., Gordon, T., Dube,
 1191 W. P., McKeen, S. A., Brioude, J., Ahmadov, R., Bougiatioti, A., Lin, J. J., Nenes, A., Wolfe, G. M.,
 1192 Hanisco, T. F., Lee, B. H., Lopez-Hilfiker, F. D., Thornton, J. A., Keutsch, F. N., Kaiser, J., Mao, J.,
 1193 and Hatch, C. D.: Instrumentation and measurement strategy for the NOAA SENEX aircraft
 1194 campaign as part of the Southeast Atmosphere Study 2013, *Atmos. Meas. Tech.*, 9, 3063–3093,
 1195 <https://doi.org/10.5194/amt-9-3063-2016>, 2016.
- 1196 Wolfe, G. M., Hanisco, T. F., Arkinson, H. L., Blake, D. R., Wisthaler, A., Mikoviny, T., Ryerson, T. B.,
 1197 Pollack, I., Peischl, J., Wennberg, P. O., Crouse, J. D., St. Clair, J. M., Teng, A., Huey, L. G., Liu, X.,
 1198 Fried, A., Weibring, P., Richter, D., Walega, J., Hall, S. R., Ullmann, K., Jimenez, J. L., Campuzano-
 1199 Jost, P., Bui, T. P., Diskin, G., Podolske, J. R., Sachse, G., and Cohen, R. C.: Photochemical evolution
 1200 of the 2013 California Rim Fire: synergistic impacts of reactive hydrocarbons and enhanced oxidants,
 1201 *Atmos. Chem. Phys.*, 22, 4253–4275, <https://doi.org/10.5194/acp-22-4253-2022>, 2022.

- 1202 Wolfe, G. M., Marvin, M. R., Roberts, S. J., Travis, K. R., and Liao, J.: The Framework for 0-D
1203 Atmospheric Modeling (F0AM) v3.1, *Geosci. Model Dev.*, 9, 3309–3319,
1204 <https://doi.org/10.5194/gmd-9-3309-2016>, 2016.
- 1205 Wu, Y., Zhao, K., Ren, X., Dickerson, R. R., Huang, J., Schwab, M. J., Stratton, P. R., Daley, H., Li, D.,
1206 and Moshary, F.: Ozone pollution episodes and PBL height variation in the NYC urban and coastal
1207 areas during LISTOS 2019, *Atmos. Environ.*, 320, 120317,
1208 <https://doi.org/10.1016/j.atmosenv.2023.120317>, 2024.
- 1209 Xu, W., Zhang, G., Wang, Y., Tong, S., Zhang, W., Ma, Z., Lin, W., Kuang, Y., Yin, L., and Xu, X.:
1210 Aerosol Promotes Peroxyacetyl Nitrate Formation During Winter in the North China Plain, *Environ.*
1211 *Sci. Technol.*, 55, 3568–3581, <https://doi.org/10.1021/acs.est.0c08157>, 2021.
- 1212 Yousefian, F., Faridi, S., Azimi, F., Aghaei, M., Shamsipour, M., Yaghmaeian, K., and Hassanvand, M. S.:
1213 Temporal variations of ambient air pollutants and meteorological influences on their concentrations in
1214 Tehran during 2012–2017, *Sci. Rep.*, 10, 292, <https://doi.org/10.1038/s41598-019-56578-6>, 2020.
- 1215 Zara, M., Boersma, K. F., Eskes, H., Denier van der Gon, H., Vilà-Guerau de Arellano, J., Krol, M., van
1216 der Swaluw, E., Schuch, W., and Velders, G. J. M.: Reductions in nitrogen oxides over the
1217 Netherlands between 2005 and 2018 observed from space and on the ground: Decreasing emissions
1218 and increasing O₃ indicate changing NO_x chemistry, *Atmos. Environ.: X*, 9, 100104,
1219 <https://doi.org/10.1016/j.aeaoa.2021.100104>, 2021.
- 1220 Zhang, J., Wang, T., Chameides, W. L., Cardelino, C., Kwok, J., Blake, D. R., Ding, A., and So, K. L.:
1221 Ozone production and hydrocarbon reactivity in Hong Kong, Southern China, *Atmos. Chem. Phys.*, 7,
1222 557–573, <https://doi.org/10.5194/acp-7-557-2007>, 2007.